

A hot-Jupiter progenitor on a super-eccentric retrograde orbit

<https://doi.org/10.1038/s41586-024-07688-3>

Received: 19 January 2024

Accepted: 7 June 2024

Published online: 17 July 2024

Open access

 Check for updates

Arvind F. Gupta^{1,2,3✉}, Sarah C. Millholland^{4,5}, Haedam Im^{4,5}, Jiayin Dong⁶, Jonathan M. Jackson⁷, Ilaria Carleo^{8,9}, Jessica Libby-Roberts^{2,3}, Megan Delamer^{2,3}, Mark R. Giovannazzi¹⁰, Andrea S. J. Lin^{2,3}, Shubham Kanodia¹¹, Xian-Yu Wang¹², Keivan Stassun¹³, Thomas Masseron^{8,9}, Diana Dragomir¹⁴, Suvrath Mahadevan^{2,3}, Jason Wright^{2,3,15}, Jaime A. Alvarado-Montes^{16,17}, Chad Bender¹⁸, Cullen H. Blake¹⁰, Douglas Caldwell¹⁹, Caleb I. Cañas²⁰, William D. Cochran^{21,22}, Paul Dalba²³, Mark E. Everett¹, Pipa Fernandez¹, Eli Golub¹, Bruno Guillet³⁸, Samuel Halverson²⁴, Leslie Hebb^{25,26}, Jesus Higuera¹, Chelsea X. Huang²⁷, Jessica Klusmeyer¹, Rachel Knight³⁸, Liouba Leroux³⁸, Sarah E. Logsdon¹, Margaret Loose³⁸, Michael W. McElwain²⁰, Andrew Monson¹⁸, Joe P. Ninan²⁸, Grzegorz Nowak^{8,9,29}, Enric Palle^{8,9}, Yatrik Patel¹, Joshua Pepper³⁰, Michael Primm³⁸, Jayadev Rajagopal¹, Paul Robertson³¹, Arpita Roy³², Donald P. Schneider^{2,3}, Christian Schwab^{16,17}, Heidi Schweiker¹, Lauren Sgro¹⁹, Masao Shimizu³⁸, Georges Simard³⁸, Guðmundur Stefánsson^{33,34}, Daniel J. Stevens³⁵, Steven Villanueva²⁰, John Wisniewski³⁶, Stefan Will³⁸ & Carl Ziegler³⁷

Giant exoplanets orbiting close to their host stars are unlikely to have formed in their present configurations¹. These ‘hot Jupiter’ planets are instead thought to have migrated inward from beyond the ice line and several viable migration channels have been proposed, including eccentricity excitation through angular-momentum exchange with a third body followed by tidally driven orbital circularization^{2,3}. The discovery of the extremely eccentric ($e = 0.93$) giant exoplanet HD 80606 b (ref. 4) provided observational evidence that hot Jupiters may have formed through this high-eccentricity tidal-migration pathway⁵. However, no similar hot-Jupiter progenitors have been found and simulations predict that one factor affecting the efficacy of this mechanism is exoplanet mass, as low-mass planets are more likely to be tidally disrupted during periastron passage^{6–8}. Here we present spectroscopic and photometric observations of TIC 241249530 b, a high-mass, transiting warm Jupiter with an extreme orbital eccentricity of $e = 0.94$. The orbit of TIC 241249530 b is consistent with a history of eccentricity oscillations and a future tidal circularization trajectory. Our analysis of the mass and eccentricity distributions of the transiting-warm-Jupiter population further reveals a correlation between high mass and high eccentricity.

The Transiting Exoplanet Survey Satellite (TESS)⁹ monitored the apparent brightness of the star TIC 241249530 for 28 days during the second year of its primary mission. These data reveal a transit-like approximately 0.8% dip in brightness on 12 January 2020, the shape and depth of which were consistent with a Jupiter-sized planet passing in front of the star (Fig. 1a). To find out the nature and origin of this signal, we conducted a series of ground-based observations of TIC 241249530. We first used high-spatial-resolution speckle imaging data from NESSI¹⁰ to rule out the presence of contaminating sources and confirm that the signal was not associated with a background eclipsing-binary in the TESS aperture. We then began radial velocity (RV) observations with the NEID spectrograph¹¹, which revealed that the TESS transit was probably induced by a giant exoplanet on a highly eccentric ($e = 0.94$), long-period ($P = 167$ days) orbit. These measurements were consistent with the absence of a

transit detection when TESS re-observed this star for 27 days from December 2022 to January 2023. Further NEID measurements, supplemented by observations with the HPF¹² and HARPS-N¹³ spectrographs, were strategically scheduled to be taken when the planet was predicted to be approaching periastron and thus inducing large stellar RV variations. We attempted to detect a second transit using the global Unistellar telescope network¹⁴ in March 2023, but these efforts were unsuccessful as the ephemeris was not yet well constrained. However, RV data collected during the periastron window enabled us to more precisely predict the subsequent transit window. We captured the first half of this transit using the engineered diffuser¹⁵ on the ARCTIC imager¹⁶ on 30 August 2023 (Fig. 1b). We refined the orbit using the ARCTIC data together with further NEID observations, including several concurrent with this transit and the subsequent one on 12 February 2024. Our ensemble of photometric

A list of affiliations appears at the end of the paper.

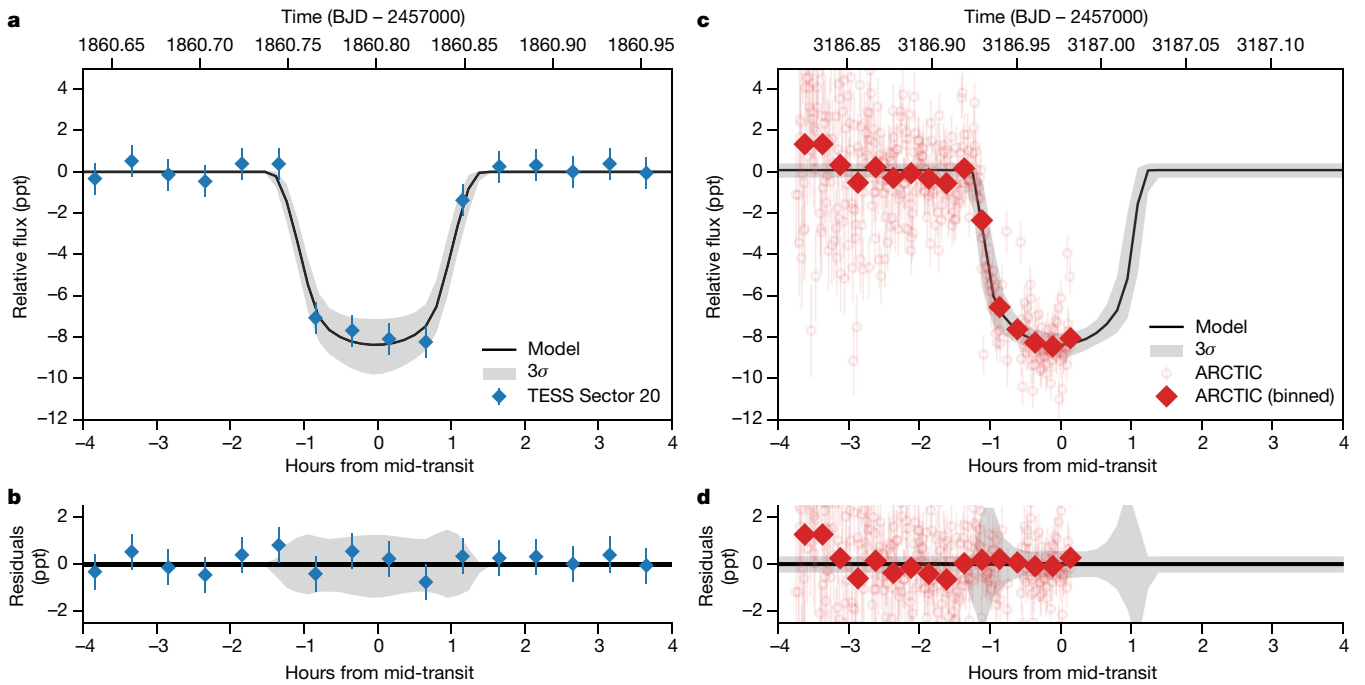


Fig. 1 | TIC 241249530 b transit measurements. **a**, TESS photometric measurements (blue), shown at their native 30-min cadence, and the best-fit transit model (black curve) and 3σ confidence region (grey). **b**, Residuals to the best-fit model for the TESS transit detection. **c**, Diffuser-assisted ARCTIC photometric measurements (red) and the best-fit transit model (black curve) and 3σ confidence region (grey). We show both the raw 30-s

cadence and binned 15-min cadence measurements, along with the residuals to the fitted transit signal. **d**, Residuals to the best-fit model for the ARCTIC transit detection. All brightnesses are given in parts per thousand (ppt). Error bars on individual data points indicate the 1σ measurement uncertainties.

and RV measurements is best explained by a massive exoplanet on a long-period, eccentric orbit.

To characterize the host star TIC 241249530, we separately analysed the NEID and HARPS-N spectra using synthetic spectral fitting techniques and we then fit the spectral energy distribution (SED; see Methods). TIC 241249530 is a main-sequence star that is slightly hotter, larger and more massive than the Sun; the derived parameters, listed in Extended Data Table 1, suggest that the star is 3.2 ± 0.5 Gyr old. The star also has a low-mass binary stellar companion, TIC 241249532, at a projected separation of $4.930 \pm 0.104''$, or $1,664 \pm 11$ AU.

We jointly fit the NEID, HPF, HARPS-N, TESS and ARCTIC measurements, accounting for perturbations to the in-transit RV signal owing to the Rossiter–McLaughlin effect. The transit and RV fits are shown in Figs. 1 and 2, respectively, and the best-fit parameters are given in Table 1. TIC 241249530 b is an exoplanet that is $4.98^{+0.16}_{-0.18}$ times as massive as Jupiter and it is on a $165.77190^{+0.00027}_{-0.00028}$ -day orbit around its host star, with an eccentricity of $0.9412^{+0.0009}_{-0.0009}$. Our fit to the Rossiter–McLaughlin signal (Fig. 2b) shows that the exoplanet is orbiting in the opposite direction to the projected stellar spin ($\lambda = 163.5^{+9.4}_{-7.7}$) and is retrograde to 99.5% confidence. Few exoplanets have orbits as extreme as this; this orbit is more eccentric than that of any other transiting exoplanet, and only a handful of known planets have similarly large projected spin–orbit misalignments¹⁷.

The planet that most closely resembles TIC 241249530 b is HD 80606 b (ref. 4), which has a mass 4.1 times that of Jupiter and is also on a misaligned orbit with a period of 111 days and an eccentricity of 0.93. HD 80606 b is an archetypal example of an exoplanet destined to become a hot Jupiter with an eventual orbital period of less than 10 days. The eccentric orbit carries the planet close enough to its host star at periastron that tides raised on the planet and star will sap energy from the orbit, causing it to gradually shrink and circularize. Also, simulations^{3,5} show that the present orbit of HD 80606 b is consistent with a

history of von Zeipel–Lidov–Kozai (vZLK) eccentricity oscillations^{18–20} driven by angular momentum exchange with HD 80607, the stellar companion to the host star. Our own simulations of the dynamical history and trajectory of TIC 241249530 b (see Methods) show that the orbit is consistent with this same type of perturber-coupled, high-eccentricity tidal migration. Eccentricity oscillations would have continued until the most recent few hundred million years, at which point general relativistic precession overtook the torque exerted by the companion, locking

Table 1 | TIC 241249530 b system parameters

Parameter	Value	Description
T_0	$2458860.8007^{+0.0015}_{-0.0016}$	Time of mid-transit (BJD)
P	$165.77190^{+0.00027}_{-0.00028}$	Orbital period (days)
e	$0.9412^{+0.0009}_{-0.0009}$	Orbital eccentricity
ω	$42.32^{+0.40}_{-0.36}$	Argument of periastron ($^\circ$)
i	$85.17^{+0.57}_{-0.51}$	Orbital inclination ($^\circ$)
K	$463.3^{+4.1}_{-4.0}$	RV semi-amplitude (ms^{-1})
M_p	$4.98^{+0.16}_{-0.18}$	Exoplanet mass (M_J)
R_p	$1.19^{+0.04}_{-0.04}$	Exoplanet radius (R_J)
λ	$163.5^{+9.4}_{-7.7}$	Projected spin–orbit obliquity ($^\circ$)
M_*	$1.27^{+0.061}_{-0.068}$	Stellar mass (M_\odot)
R_*	$1.397^{+0.025}_{-0.028}$	Stellar radius (R_\odot)
$v \sin i_*$	$4.60^{+0.56}_{-0.63}$	Projected rotational velocity (km s^{-1})

We report the median values of the posterior distributions from our joint fit to the observed transits and RVs. The uncertainties represent the 68% confidence intervals ($\pm 1\sigma$) for each parameter.

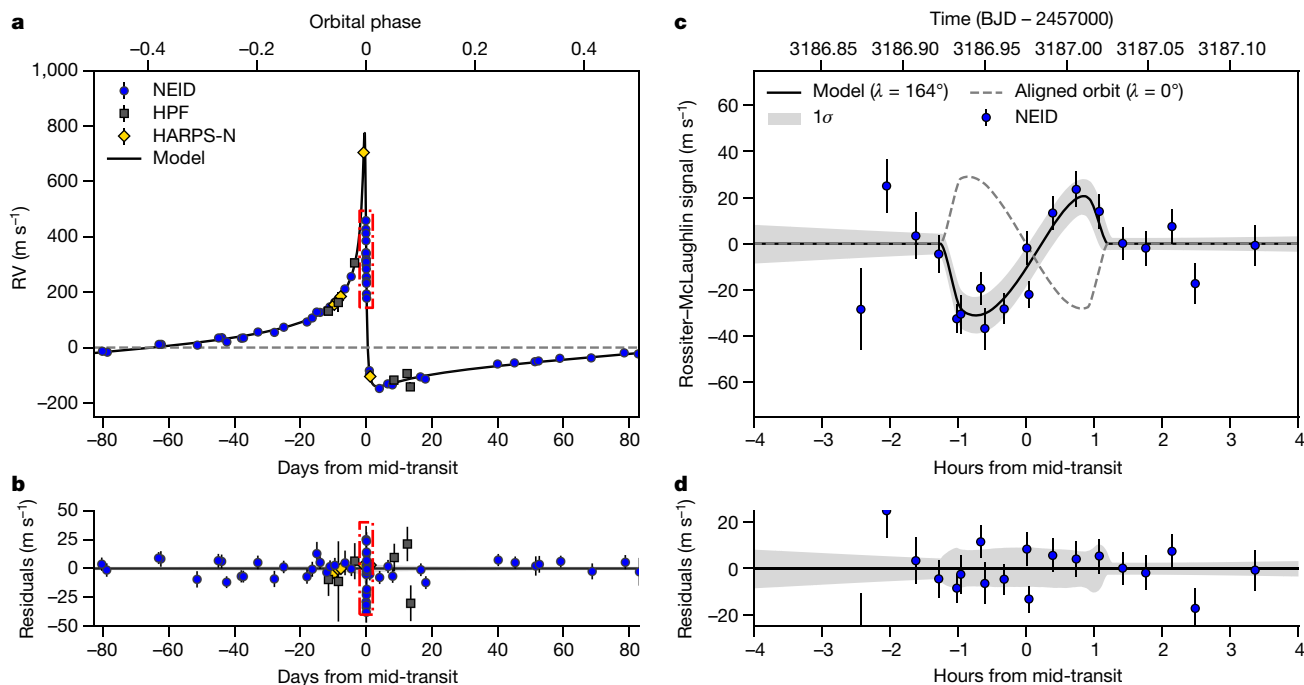


Fig. 2 | Phase-folded RV measurements for TIC 241249530. a, RV measurements from NEID (blue), HPF (black), HARPS-N (yellow) and best-fit orbit model (black curve). **b,** Residuals to the RV orbit fit. **c,** Best-fit Rossiter–McLaughlin model (solid curve) and 1σ confidence region (grey), with the signal

for aligned orbit shown for comparison (dashed curve). **d,** Residuals to the Rossiter–McLaughlin model fit. The dashed red box in **a** highlights the in-transit RV measurements, which are shown in **b**. Error bars on individual data points indicate the 1σ measurement uncertainties.

the exoplanet on an eccentric orbit that is now gradually circularizing. The architectures of the HD 80606 and TIC 241249530 systems lend support to this process as a plausible hot-Jupiter-formation mechanism. However, although other giant exoplanets on tidal migration tracks have been discovered²¹, including two that probably have vZLK-driven dynamical histories^{22,23}, no previous examples have eccentricities >0.9 and none have formation scenarios as clear as that of HD 80606 b. The observed occurrence rate of super-eccentric progenitors to hot Jupiters^{24,25} falls well short of predictions from simulations²⁶, suggesting that giant-planet migration is dominated by other channels. With the discovery of TIC 241249530 b, a second super-eccentric exoplanet in a hierarchical triple system has been added to the sparse sample, providing a new lens through which we can explore the formation of these planets.

Not only do the TIC 241249530 b and HD 80606 b systems share similar orbital architectures but these exoplanets also have similar masses. The masses and eccentricities of all transiting warm Jupiters, which we define as giant planets with intermediate periods ($10 \text{ days} < P < 365 \text{ days}$), are shown in Fig. 3b. These two planets, which are the only members of the sample with super-eccentric orbits ($e > 0.9$), are also among the most massive. A correlation between exoplanet mass and eccentricity has been identified in previous works^{27–30}, each of which found that higher-mass planets are more likely to have larger orbital eccentricities. We find that our narrower sample of transiting giant planets conforms to this known trend (see Methods); the eccentricity distributions of high-mass ($M_p > 2 M_J$) and low-mass ($0.3 M_J \leq M_p \leq 2 M_J$) members of this population are statistically distinct (Fig. 3a). Although lower-mass planets are more likely to be found on low-eccentricity orbits, high-mass planets exhibit a broad, nearly flat distribution from circular to highly eccentric orbits.

Although the observed mass–eccentricity correlation may be shaped by several processes, such as collisional eccentricity growth³⁰ or resonant interactions with the protoplanetary disk^{31–33}, the high masses

of TIC 241249530 b and HD 80606 b may offer a clue as to the death of super-eccentric giant planets. During the high-eccentricity phase of vZLK oscillations, orbital eccentricities can be driven so close to unity that the exoplanet will approach, or even breach, the tidal radius of the host star. Because the tidal radius is inversely proportional to the planet–star mass ratio, lower-mass planets more easily cross this threshold and experience tidal disruption. A relative dearth of low-mass, eccentric progenitors to hot Jupiters is a consistent outcome of simulations of high-eccentricity tidal migration following vZLK oscillations under an equilibrium tide assumption^{6–8}. For planets susceptible to chaotic, or diffusive, dynamical tidal evolution, whereby oscillations excited in the planet accelerate orbital decay, this mass dependence is largely erased, as low-mass planets can become decoupled from the perturber before being disrupted³⁴. However, chaotic tides facilitate circularization on a much shorter timescale ($<100 \text{ Myr}$); these planets will spend very little time with intermediate-period orbits^{34–36}. It is possible that only the most massive eccentric giant planets last long enough in this period regime to be represented in the observed sample.

TIC 241249530 b passes through periastron just six hours before each transit, presenting a unique opportunity to observe how an exoplanet atmosphere responds to a rapid, extreme heating event. Temporal variations in exoplanet atmospheres are best explored through studies of planets on eccentric orbits, for which we may see signatures of time-varying irradiation and changing pressure–temperature profiles, such as turbulent surface flows³⁷ and disequilibrium chemistry³⁸, depending on the heat-redistribution timescales. The atmospheres of several eccentric giant planets have been studied^{39–41}, but the periastron phase has not been captured in transit for these systems. The orbital geometry of TIC 241249530 b will make such measurements possible for the first time. The planetary atmosphere can also be studied by means of emission measurements during other orbital phases, but the orientation precludes a secondary eclipse at a 6.3σ confidence.

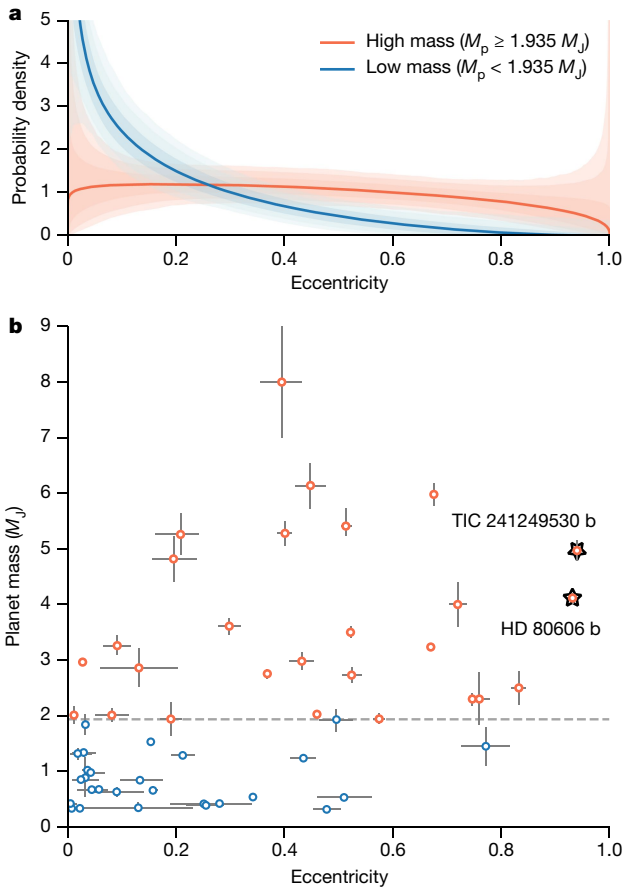


Fig. 3 | Mass–eccentricity distribution for transiting warm Jupiters. **a**, Best-fit beta distributions for transiting warm Jupiters more massive (red) and less massive (blue) than $1.935 M_J$. The shaded regions represent the 1σ (darkest), 2σ and 3σ (lightest) posteriors on each fit. **b**, Masses and eccentricities of transiting warm Jupiters. The super-eccentric hot-Jupiter progenitors HD 80606 b and TIC 241249530 b are labelled with upright and inverted stars, respectively. The horizontal dashed line indicates the median mass of the population, which is the threshold used for the fits shown in **a**. Our results are insensitive to the exact value of the threshold (see Methods); the median is chosen simply for visualization purposes. Error bars on individual data points indicate the 1σ uncertainties from the literature.

Online content

Any methods, additional references, Nature Portfolio reporting summaries, source data, extended data, supplementary information, acknowledgements, peer review information; details of author contributions and competing interests; and statements of data and code availability are available at <https://doi.org/10.1038/s41586-024-07688-3>.

- Dawson, R. I. & Johnson, J. A. Origins of hot Jupiters. *Annu. Rev. Astron. Astrophys.* **56**, 175–221 (2018).
- Holman, M., Touma, J. & Tremaine, S. Chaotic variations in the eccentricity of the planet orbiting 16 Cygni B. *Nature* **386**, 254–256 (1997).
- Fabrycky, D. & Tremaine, S. Shrinking binary and planetary orbits by Kozai cycles with tidal friction. *Astrophys. J.* **669**, 1298–1315 (2007).
- Naef, D. et al. HD 80606 b, a planet on an extremely elongated orbit. *Astron. Astrophys.* **375**, L27–L30 (2001).
- Wu, Y. & Murray, N. Planet migration and binary companions: the case of HD 80606b. *Astrophys. J.* **589**, 605–614 (2003).
- Petrovich, C. Steady-state planet migration by the Kozai-Lidov mechanism in stellar binaries. *Astrophys. J.* **799**, 27 (2015).
- Anderson, K. R., Storch, N. I. & Lai, D. Formation and stellar spin-orbit misalignment of hot Jupiters from Lidov–Kozai oscillations in stellar binaries. *Mon. Not. R. Astron. Soc.* **456**, 3671–3701 (2016).
- Muñoz, D. J., Lai, D. & Liu, B. The formation efficiency of close-in planets via Lidov–Kozai migration: analytic calculations. *Mon. Not. R. Astron. Soc.* **460**, 1086–1093 (2016).
- Ricker, G. R. et al. Transiting Exoplanet Survey Satellite (TESS). *J. Astron. Telesc. Instrum. Syst.* **1**, 014003 (2015).

- Scott, N. J. et al. The NN-exlore Exoplanet Stellar Speckle Imager: instrument description and preliminary results. *Publ. Astron. Soc. Pac.* **130**, 054502 (2018).
- Schwab, C. et al. Design of NEID, an extreme precision Doppler spectrograph for WIYN. *Proc. SPIE* **9908**, 99087H (2016).
- Mahadevan, S. et al. The Habitable-zone Planet Finder: a stabilized fiber-fed NIR spectrograph for the Hobby-Eberly Telescope. *Proc. SPIE* **8446**, 844615 (2012).
- Cosentino, R. et al. Harps-N: the new planet hunter at TNG. *Proc. SPIE* **8446**, 84461V (2012).
- Peluso, D. O. et al. The Unistellar Exoplanet Campaign: citizen science results and inherent education opportunities. *Publ. Astron. Soc. Pac.* **135**, 015001 (2023).
- Stefánsson, G. et al. Toward space-like photometric precision from the ground with beam-shaping diffusers. *Astrophys. J.* **848**, 9 (2017).
- Huehnerhoff, J. et al. Astrophysical Research Consortium Telescope Imaging Camera (ARCTIC) facility optical imager for the Apache Point Observatory 3.5m telescope. *Proc. SPIE* **9908**, 99085H (2016).
- Albrecht, S. H., Dawson, R. I. & Winn, J. N. Stellar obliquities in exoplanetary systems. *Publ. Astron. Soc. Pac.* **134**, 082001 (2022).
- von Zeipel, H. Sur l'application des séries de M. Lindstedt à l'étude du mouvement des comètes périodiques. *Astron. Nachr.* **183**, 345 (1910).
- Lidov, M. L. The evolution of orbits of artificial satellites of planets under the action of gravitational perturbations of external bodies. *Planet. Space Sci.* **9**, 719–759 (1962).
- Kozai, Y. Secular perturbations of asteroids with high inclination and eccentricity. *Astron. J.* **67**, 591–598 (1962).
- Dong, J. et al. TOI-3362b: a proto hot Jupiter undergoing high-eccentricity tidal migration. *Astrophys. J. Lett.* **920**, L16 (2021).
- Barbieri, M. et al. HD 17156b: a transiting planet with a 21.2-day period and an eccentric orbit. *Astron. Astrophys.* **476**, L13–L16 (2007).
- Santerne, A. et al. SOPHIE velocimetry of Kepler transit candidates. XII. KOI-1257 b: a highly eccentric three-month period transiting exoplanet. *Astron. Astrophys.* **571**, A37 (2014).
- Dawson, R. I., Murray-Clay, R. A. & Johnson, J. A. The photoeccentric effect and proto-hot Jupiters. III. A paucity of proto-hot Jupiters on super-eccentric orbits. *Astrophys. J.* **798**, 66 (2015).
- Jackson, J. M. et al. Statistical analysis of the dearth of super-eccentric Jupiters in the Kepler sample. *Astron. J.* **165**, 82 (2023).
- Socrates, A. et al. Super-eccentric migrating Jupiters. *Astrophys. J.* **750**, 106 (2012).
- Butler, R. P. et al. Catalog of nearby exoplanets. *Astrophys. J.* **646**, 505–522 (2006).
- Ford, E. B. & Rasio, F. A. Origins of eccentric extrasolar planets: testing the planet-planet scattering model. *Astrophys. J.* **686**, 621–636 (2008).
- Wright, J. T. et al. Ten new and updated multiplanet systems and a survey of exoplanetary systems. *Astrophys. J.* **693**, 1084–1099 (2009).
- Freikh, R. et al. Signatures of a planet–planet impacts phase in exoplanetary systems hosting giant planets. *Astrophys. J. Lett.* **884**, L47 (2019).
- Papaloizou, J. C. B., Nelson, R. P. & Masset, F. Orbital eccentricity growth through disc-companion tidal interaction. *Astron. Astrophys.* **366**, 263–275 (2001).
- Goldreich, P. & Sari, R. Eccentricity evolution for planets in gaseous disks. *Astrophys. J.* **585**, 1024–1037 (2003).
- Romanova, M. M. et al. Eccentricity growth of massive planets inside cavities of protoplanetary discs. *Mon. Not. R. Astron. Soc.* **523**, 2832–2849 (2023).
- Vick, M., Lai, D. & Anderson, K. R. Chaotic tides in migrating gas giants: forming hot and transient warm Jupiters via Lidov–Kozai migration. *Mon. Not. R. Astron. Soc.* **484**, 5645–5668 (2019).
- Wu, Y. Diffusive tidal evolution for migrating hot Jupiters. *Astron. J.* **155**, 118 (2018).
- Rozner, M. et al. Inflated eccentric migration of evolving gas giants I – accelerated formation and destruction of hot and warm Jupiters. *Astrophys. J.* **931**, 10 (2022).
- Langton, J. & Laughlin, G. Hydrodynamic simulations of unevenly irradiated Jovian planets. *Astrophys. J.* **674**, 1106–1116 (2008).
- Mayorga, L. C. et al. Variable irradiation on 1D cloudless eccentric exoplanet atmospheres. *Astrophys. J.* **915**, 41 (2021).
- Laughlin, G. et al. Rapid heating of the atmosphere of an extrasolar planet. *Nature* **457**, 562–564 (2009).
- Lewis, N. K. et al. Orbital phase variations of the eccentric giant planet HAT-P-2b. *Astrophys. J.* **766**, 95 (2013).
- de Wit, J. et al. Direct measure of radiative and dynamical properties of an exoplanet atmosphere. *Astrophys. J. Lett.* **820**, L33 (2016).

Publisher's note Springer Nature remains neutral with regard to jurisdictional claims in published maps and institutional affiliations.



Open Access This article is licensed under a Creative Commons Attribution 4.0 International License, which permits use, sharing, adaptation, distribution and reproduction in any medium or format, as long as you give appropriate credit to the original author(s) and the source, provide a link to the Creative Commons licence, and indicate if changes were made. The images or other third party material in this article are included in the article's Creative Commons licence, unless indicated otherwise in a credit line to the material. If material is not included in the article's Creative Commons licence and your intended use is not permitted by statutory regulation or exceeds the permitted use, you will need to obtain permission directly from the copyright holder. To view a copy of this licence, visit <http://creativecommons.org/licenses/by/4.0/>.

© The Author(s) 2024

¹U.S. National Science Foundation National Optical-Infrared Astronomy Research Laboratory (NSF NOIRLab), Tucson, AZ, USA. ²Department of Astronomy and Astrophysics, The Pennsylvania State University, University Park, PA, USA. ³Center for Exoplanets and Habitable Worlds, The Pennsylvania State University, University Park, PA, USA. ⁴Department of Physics,

Massachusetts Institute of Technology, Cambridge, MA, USA. ⁵Kavli Institute for Astrophysics and Space Research, Massachusetts Institute of Technology, Cambridge, MA, USA. ⁶Center for Computational Astrophysics, Flatiron Institute, New York, NY, USA. ⁷Van Vleck Observatory, Astronomy Department, Wesleyan University, Middletown, CT, USA. ⁸Instituto de Astrofísica de Canarias (IAC), La Laguna, Tenerife, Spain. ⁹Departamento de Astrofísica, Universidad de La Laguna (ULL), La Laguna, Tenerife, Spain. ¹⁰Department of Physics and Astronomy, University of Pennsylvania, Philadelphia, PA, USA. ¹¹Earth and Planets Laboratory, Carnegie Institution for Science, Washington DC, USA. ¹²Department of Astronomy, Indiana University Bloomington, Bloomington, IN, USA. ¹³Department of Physics and Astronomy, Vanderbilt University, Nashville, TN, USA. ¹⁴Department of Physics and Astronomy, University of New Mexico, Albuquerque, NM, USA. ¹⁵Penn State Extraterrestrial Intelligence Center, The Pennsylvania State University, University Park, PA, USA. ¹⁶School of Mathematical and Physical Sciences, Macquarie University, North Ryde, New South Wales, Australia. ¹⁷The Macquarie University Astrophysics and Space Technologies Research Centre, Macquarie University, North Ryde, New South Wales, Australia. ¹⁸Department of Astronomy and Steward Observatory, University of Arizona, Tucson, AZ, USA. ¹⁹Carl Sagan Center, SETI Institute, Mountain View, CA, USA. ²⁰NASA Goddard Space Flight Center, Greenbelt, MD, USA. ²¹Center for Planetary Systems

Habitability, The University of Texas at Austin, Austin, TX, USA. ²²McDonald Observatory, The University of Texas at Austin, Austin, TX, USA. ²³Department of Astronomy and Astrophysics, University of California, Santa Cruz, Santa Cruz, CA, USA. ²⁴Jet Propulsion Laboratory, California Institute of Technology, Pasadena, CA, USA. ²⁵Physics Department, Hobart and William Smith Colleges, Geneva, NY, USA. ²⁶Department of Astronomy, Cornell University, Ithaca, NY, USA. ²⁷Centre for Astrophysics, University of Southern Queensland, Toowoomba, Queensland, Australia. ²⁸Department of Astronomy and Astrophysics, Tata Institute of Fundamental Research, Mumbai, India. ²⁹Institute of Astronomy, Faculty of Physics, Astronomy and Informatics, Nicolaus Copernicus University, Toruń, Poland. ³⁰Department of Physics, Lehigh University, Bethlehem, PA, USA. ³¹Department of Physics & Astronomy, University of California, Irvine, Irvine, CA, USA. ³²Schmidt Sciences, New York, NY, USA. ³³Department of Astrophysical Sciences, Princeton University, Princeton, NJ, USA. ³⁴Anton Pannekoek Institute for Astronomy, University of Amsterdam, Amsterdam, The Netherlands. ³⁵Department of Physics & Astronomy, University of Minnesota Duluth, Duluth, MN, USA. ³⁶NASA Headquarters, Washington DC, USA. ³⁷Department of Physics, Engineering & Astronomy, Stephen F. Austin State University, Nacogdoches, TX, USA. ³⁸Unaffiliated: Bruno Guillet, Rachel Knight, Liouba Leroux, Margaret Loose, Michael Primm, Masao Shimizu, Georges Simard, Stefan Will. ³⁹e-mail: arvind.gupta@noirlab.edu

Methods

TESS photometry

TIC 241249530 was observed with TESS⁹ from 24 December 2019 to 21 January 2020 (Sector 20) at a 30-min cadence and from 21 December 2022 to 18 January 2023 (Sector 60) at a 2-min cadence. A single transit-like dip (flux depth about 8 parts per thousand) was identified by the TESS Single Transit Planet Candidate Working Group (TSTPC WG) in the Sector 20 Quick Look Pipeline^{42,43} light curve using a box least-squares search. The TSTPC WG focuses on searching full-frame TESS light curves for isolated transit events and validating and confirming those that are true planets, with the aim of increasing the yield of TESS planets with period >30 days (for example, refs. 44–47). There is no flux centroid motion during the transit event for TIC 241249530 and we identify no other sources brighter than $\Delta m_G = 5$ in the target aperture. Although there is flux contamination from two nearby stars with $6 > \Delta m_G > 5$, TIC 241249532 and TIC 241249533, both of which were centred on the same pixel as TIC 241249530 in Sector 20, these are too faint to have been responsible for the observed change in brightness. No notable brightness variations were detected in the Sector 60 light curve. For all subsequent analysis in this work, we rely on the pre-search data conditioned simple aperture photometry^{48–50} (PDCSAP) light curve from the Science Processing Operations Center⁵¹ (SPOC) for Sector 60 and the TESS-SPOC⁵² light curve for Sector 20 (Extended Data Fig. 1).

High-contrast imaging

To verify that the transit signature detected by TESS was indeed associated with TIC 241249530 and not with a nearby star or binary system that was blended in the TESS aperture, we used the NN-EXPLORE Exoplanet Stellar Speckle Imager (NESSI)¹⁰ on the WIYN 3.5-m telescope at Kitt Peak National Observatory to conduct high-spatial-resolution observations of the target on 21 April 2021. A sequence of 1,000 40-ms exposures was taken in the 832-nm and 562-nm narrow-band filters simultaneously with the red and blue NESSI cameras, respectively. These diffraction-limited exposures were used to reconstruct high-contrast images (Extended Data Fig. 2) following the steps outlined in ref. 53. The achieved 5σ contrast limits are sufficient to rule out the presence of faint stellar companions and background sources with $\Delta \text{mag}_{562} < 3.3$ and $\Delta \text{mag}_{832} < 3.7$ at a separation of $0.2''$ and $\Delta \text{mag}_{562} < 3.9$ and $\Delta \text{mag}_{832} < 4.8$ at a separation of $1''$.

Ground-based photometric observations

We used the Unistellar Network, a collaboration of citizen scientists using Unistellar telescopes⁵⁴ in support of astronomical research, to observe TIC 241249530 from locations in Japan, Europe and the United States in search for transit signatures in March 2023. Observations were taken at various times from 7 to 19 March 2023, when the companion orbital period and transit ephemeris were still highly uncertain. After removing off-target and saturated frames, we calibrated the remaining images, binned them in sets of 15–30 to amplify the signal-to-noise ratio (S/N) and performed differential photometry^{55,56}. No signatures of statistical significance were found in the Unistellar data and, based on our subsequent orbit fit, we confirm that none of these observations were taken during the transit.

We observed TIC 241249530 again on 30 August 2023 with the Astrophysical Research Consortium Telescope Imaging Camera (ARCTIC)¹⁶ on the ARC 3.5-m telescope at Apache Point Observatory (APO). Observations were conducted using a beam-shaping diffuser, which creates a stable top-hat point spread function of the star to improve photometric precision¹⁵. We used the Semrock narrow-band filter (838–876 nm) to avoid atmospheric absorption bands⁵⁷. We began observing when the target rose above an air mass of 4 (altitude $\approx 10^\circ$) and continued until 12⁰⁰ morning twilight, collecting a continuous 4.3-h baseline of consecutive 30-s exposures. As the star rose above air mass approximately 1.5, about

2.5 h after the start of the observing sequence, a transit-like decrease in brightness was observed.

To reduce the ARCTIC data, a median-combined master bias image was constructed and subtracted from the individual science frames, which were flat-fielded using dome flat exposures taken at the start of the night. We performed differential aperture photometry on the reduced data using AstroImageJ⁵⁸ with a 17-pixel ($7.7''$) aperture and four reference stars that were carefully selected to minimize the scatter of the out-of-transit flux. Flux uncertainties were calculated following the procedures in refs. 15,59, which account for photon noise from the star and background, detector read noise and air-mass-dependent scintillation noise. We removed exposures flagged by AstroImageJ for approaching the detector saturation limit, as well as exposures taken during intermittent cloud cover that introduced further scatter.

The diffused point spread function of TIC 241249530 overlapped with that of TIC 241249532. Before initiating our ARCTIC observing sequence, we collected several individual exposures without the diffuser in the optical path. We used these data to calculate the relative brightness contributions of the two stars. TIC 241249532 contributes just 0.53% of the total flux in the Semrock bandpass.

Spectroscopic observations

We monitored the RV signal of TIC 241249530 with the NEID spectrograph¹¹ on the WIYN 3.5-m telescope, collecting measurements on 40 separate nights between 2 September 2021 and 1 March 2024. On all but three of these nights, single exposures were taken, with exposure times ranging from 500 to 1,800 s, depending on the observing conditions. On the night of 30 August 2023, four consecutive 20-min exposures were taken simultaneously with the partial transit as observed with ARCTIC, and on the subsequent night, we secured a pair of measurements separated by an hour. We also obtained a sequence of 15 consecutive 20-min exposures on the night of 12 February 2024; this sequence covered a full transit as well as several measurements before ingress and after egress. We discard two spectra that were taken on nights for which the wavelength calibration was identified to be unreliable, leaving us with 56 high-quality measurements with a median S/N per extracted pixel of 25 at 550 nm. The raw echelle spectra were processed with version 1.3 of the NEID Data Reduction Pipeline (DRP; <https://neid.ipac.caltech.edu/docs/NEID-DRP/>), which produces wavelength-calibrated 1D spectra and then calculates RVs using the cross-correlation function (CCF) method⁶⁰. We also independently calculated the RVs from the calibrated 1D spectra using a modified version of the SpEctrum Radial Velocity AnaLyser (SERVAL) template-matching algorithm^{61,62} that has been optimized for NEID spectra as described by ref. 63. The SERVAL RVs were calculated using the central 7,000 pixels of 79 orders centred between 4,010 and 8,400 Å (order indices 20 to 100, corresponding to echelle orders 153 to 73). The template-matching results outperform the CCF-based RVs from the NEID DRP, with median single measurement precisions of $\sigma_{\text{RV,SERVAL}} = 6.3 \text{ m s}^{-1}$ and $\sigma_{\text{RV,DRP}} = 7.9 \text{ m s}^{-1}$, so we chose to use the SERVAL RVs for the analysis performed in this work.

Further RV measurements were taken with the Habitable-zone Planet Finder (HPF) spectrograph¹², which is on the Hobby–Eberly Telescope (HET)^{64,65} at McDonald Observatory, and the HARPS-N spectrograph, mounted on Telescopio Nazionale Galileo (TNG) in La Palma, as TIC 241249530 approached periastron in March 2023. Six HPF observations were made between 6 and 31 March 2023, for which each observation consisted of two consecutive 945-s exposures with a median nightly binned S/N per extracted pixel of 137 at 1,000 nm. These data were processed using the HxRGproc⁶⁶ and barycorrpy⁶⁷ packages and the RVs were calculated using a version of SERVAL that has been modified for HPF^{68,69}. We achieve a median RV measurement precision of 15.0 m s^{-1} . We also observed the target five times with HARPS-N between 7 and 18 March 2023, with an exposure time of 3,300 s and a mean (min, max) S/N of 55 (37, 75). We reduced the data with the offline version of the HARPS-N data-reduction software through the Yabi web

interface⁷⁰ installed at the Italian Center for Astronomical Archives Data Center. To extract the RVs, we used a G2 mask template and obtained a CCF width of 9.9 km s^{-1} , with an average precision of 0.1 km s^{-1} . The median resulting RV measurement precision is 3.4 m s^{-1} . We show the complete RV time series from NEID, HPF and HARPS-N in Extended Data Fig. 3.

Stellar characterization of TIC 241249530

To determine the stellar atmospheric parameters of TIC 241249530, we analysed the out-of-transit NEID spectra collected before September 2023 (cumulative S/N ≈ 100 at 550 nm) using the iSpec^{71,72} Python package to perform synthetic spectral fitting. We used the SPECTRUM radiative transfer code⁷³, MARCS atmospheric models⁷⁴, solar abundances from 3D hydrodynamic models⁷⁵ and the sixth version of the Gaia ESO survey (GES) atomic line list⁷⁶. The microturbulence velocity was treated as a free parameter to allow for flexibility in accounting for small-scale motions in the stellar atmosphere. Macroturbulence was determined using an empirical relation, making use of established correlations with other stellar properties⁷⁷. To streamline the fitting, we restricted the analysis to specific spectral regions from 480 to 680 nm, encompassing the wing segments of the H α , H β and Mg I triplet lines, which are sensitive to T_{eff} and $\log g$, and the Fe I and Fe II lines, which provide precise constraints on [Fe/H] and $\nu \sin i_*$. We minimize the difference between the synthetic and input spectra by applying the nonlinear least-squares Levenberg–Marquardt fitting algorithm, using constraints from the aforementioned models and line lists.

The HARPS-N spectra were independently analysed with BACCHUS⁷⁸, using MARCS atmospheric models, the GES atomic line list and the TURBOSPECTRUM radiative transfer code^{79,80}. For our fit, we constrained T_{eff} by requiring Fe I line abundances to be uncorrelated with their respective excitation potentials in the synthetic spectrum and we constrained $\log g$ by requiring ionization balance for the Fe I and Fe II lines. We also required the Fe I line abundances to be uncorrelated with their equivalent widths and the stellar metallicity ([Fe/H]) was calculated as the average of these abundances. The projected rotational velocity was estimated by fitting the broadening of the Fe I lines, accounting for the best-fit microturbulence and assuming the same macroturbulence contribution as in the iSpec analysis. The stellar parameters derived from the NEID and HARPS-N spectra are largely in good agreement ($< 1\sigma$). Discrepancies between the [Fe/H] values and $\nu \sin i_*$ values at the 1.2σ level probably result from differences between the fitted microturbulence, which is known to exhibit small variations for different fitting methods⁷². We adopt the iSpec T_{eff} , $\log g$, [Fe/H] and $\nu \sin i_*$ for the rest of the analysis in this work.

We performed an analysis of the broadband SED of TIC 241249530 together with the Gaia DR3 parallax following the procedures described in refs. 81–83. We use JHK_s magnitudes from 2MASS⁸⁴, W1–W3 magnitudes from WISE⁸⁵, $G_{\text{BP}}G_{\text{RP}}$ magnitudes from Gaia⁸⁶, BVgr magnitudes from APASS⁸⁷ and the NUV magnitude from GALEX⁸⁸. We also used the Gaia spectrophotometry spanning 0.4–1.0 μm . Altogether, the available photometry spans the full stellar SED over the wavelength range 0.2–10.0 μm . We fit the SED using PHOENIX stellar atmosphere models⁸⁹, with the effective temperature, surface gravity and metallicity set to the spectroscopically determined values. The remaining free parameter is the extinction (A_V), which we limited to the maximum line-of-sight value of $A_V = 0.44 \text{ mag}$ from galactic dust maps⁹⁰. The resulting fit is shown in Extended Data Fig. 4. Integrating the unreddened model SED yields the bolometric flux at Earth, $F_{\text{bol}} = 7.19 \pm 0.20 \times 10^{-10} \text{ erg s}^{-1} \text{ cm}^{-2}$. Taking the F_{bol} and T_{eff} together with the Gaia parallax, we calculate the stellar radius to be $R_* = 1.404 \pm 0.028 R_{\odot}$. Also, the stellar mass is inferred using empirical relations⁹¹, giving $M_* = 1.24 \pm 0.07 M_{\odot}$, and we estimate the age to be $3.2 \pm 0.5 \text{ Gyr}$ by fitting the evolutionary state with the Yonsei–Yale isochrone models⁹². Our reported 0.5-Gyr uncertainty accounts for the uncertainties on each of the inputs to the isochrone fit: effective temperature, surface

gravity, metallicity and stellar mass. However, this does not account for systematic uncertainties arising from our choice of stellar models, which can be on the order of 1 Gyr.

The best-fit extinction for our SED model is $A_V = 0.31 \pm 0.02$. This large value is supported by a clear detection of interstellar absorption in the Na D doublet and the K I 770 nm lines in the NEID spectra. Both spectroscopic analyses yield T_{eff} values that are substantially hotter than the literature value from Gaia DR3 spectrophotometric analysis⁹², which is consistent with the effect of reddening from dust along the line of sight to the star.

Using the projected rotational velocity and stellar radius, we place an upper limit on the rotation period of $16.9_{-2.6}^{+3.8} \text{ days}$. We attempt to make a more precise measurement of the rotation period to determine the stellar inclination, but the existing data are insufficient. An analysis of the TESS light curves using the TESS Systematics-Insensitive Periodogram package⁹³ shows no notable photometric modulation on timescales shorter than the length of each individual sector. We also examine archival photometry of the star from the WASP survey⁹⁴. These data consist of 2,178 measurements on 33 nights, with two isolated epochs in April 2006 and March 2007, and the remaining data covering October 2007 to March 2008. In spite of the substantially longer baseline than TESS, a Lomb–Scargle periodogram analysis of the WASP measurements reveals no notable peaks besides the half-day, one-day and two-day sampling aliases. The lack of photometric modulation is reflected in the spectroscopic data as well; we do not detect periodic variation in the activity-sensitive Ca II H & K, Na I or H α spectral lines as measured by the NEID DRP. Also, there is no emission in the Ca II H & K line cores in the NEID and HARPS-N spectra, suggesting that the star is chromospherically quiet.

Stellar characterization of TIC 241249532

TIC 241249530 shares a common parallax and proper motion with TIC 241249532 as measured by Gaia, and the two stars are separated on the sky by $4.930 \pm 0.104''$ (ref. 86). The probability of a chance alignment between TIC 241249530 and TIC 241249532 is $R = 9.73 \times 10^{-5}$ (ref. 95), suggesting that the pair is indeed gravitationally bound. Gaia’s photometric measurements of TIC 241249532 place it firmly along the main sequence. We do not perform an independent SED analysis on this star but instead estimate its mass using empirical mass–luminosity relations^{96,97}. We calculate the mass to be 0.453 ± 0.012 times that of the Sun based on the 2MASS K_s -band magnitude and 0.400 ± 0.016 times that of the Sun based on the Gaia G_{RP} -band magnitude. The stellar mass, coordinates and broadband photometry are given in Extended Data Table 1.

On the basis of the weighted mean of the Gaia parallax measurements for the system, the on-sky separation corresponds to a projected physical separation of $1,664.00 \pm 10.85 \text{ AU}$. The relative motions of these two stars are not constrained well enough by Gaia to meaningfully estimate an orbital solution. However, as an effort to quantify the dynamical impact of TIC 241249532 in our analysis, we simulated 10 million orbits sampled randomly in phase, uniformly in $\cos i$ and thermally ($f(e) = 2e$) in eccentricity. We determine the orbital period of the system to be $> 10,000$ years, with a peak in frequency at 35,000 years. Long-period stellar companions such as this can directly bias RV analyses of exoplanets in the form of a linear RV slope. However, our simulations show that TIC 241249532 probably induces a linear trend in the observed RVs of TIC 241249530 at the level of just $1 \text{ cm s}^{-1} \text{ year}^{-1}$, with 99% of our orbits returning slopes $< 30 \text{ cm s}^{-1} \text{ year}^{-1}$. The amplitude of this signal is small compared with the km s^{-1} -level variations induced by TIC 241249530 b and we therefore do not include it as an extra body in our joint fitting.

Joint transit + RV analysis

We use the exoplanet software package⁹⁸ to fit a transit model and a Keplerian orbit with Rossiter–McLaughlin perturbations to the observed photometric and RV signals for TIC 241249530. The exoplanet

package relies on `starry`^{99,100} and the underlying analytic models from ref. 101 to fit the transits, and the orbital parameter posteriors are sampled using the `PyMC3` Hamiltonian Monte Carlo package¹⁰². The orbit model consists of a full Keplerian with tight Gaussian priors on the orbital period, P , and time of conjunction, T_o , broad uniform priors on the exoplanet mass, M_p , transit impact parameter, b , and transit depth, δ , and Gaussian priors on the stellar mass, M_* , and radius, R_* . We reparameterize the eccentricity, e , and argument of periastron, ω , as $\sqrt{e} \sin \omega$ and $\sqrt{e} \cos \omega$ and we sample these on the unit disk. We do not impose an extra eccentricity prior, as the global warm-Jupiter eccentricity distribution is not well constrained¹⁰³. Separate quadratic limb-darkening coefficients, reparameterized as q_1 and q_2 as in ref. 104, are used for each instrument for which in-transit observations were taken (TESS, ARCTIC, NEID). For the RV data, we fit individual zero-point offset terms (σ) and jitter terms (γ) for each instrument, splitting the NEID RVs into two separate datasets before and after the instrument restart. Dilution terms are included for both TESS and ARCTIC, as both transit measurements suffered from flux contamination. The TESS data products already account for dilution, but previous works have demonstrated that these results are susceptible to overcorrection^{105,106}, so we allow the TESS dilution term to float uniformly from 0.1 to 1.2. For ARCTIC, we fix the dilution to be 0.9947 based on the out-of-transit data for which the target was well resolved from its companion. To model the Rossiter–McLaughlin signal, we adopt the formalism of ref. 107 along with their prior distributions for the Gaussian line dispersion parameter, β , the Lorentzian line dispersion parameter, γ , and macroturbulence, ζ . We place a Gaussian prior on the projected stellar rotational velocity, $v \sin i_*$, and a uniform prior on the projected spin-orbit misalignment, λ . The prior distributions and posterior results for all of these fit parameters, as well as for some derived values, are given in Extended Data Table 2.

Stellar obliquity

The stellar obliquity, ψ , is related to the projected obliquity, λ , by

$$\cos \psi = \sin i_* \sin i \cos \lambda + \cos i_* \cos i.$$

Here i_* is the inclination of the stellar spin axis and i is the inclination of the exoplanet orbit. We cannot directly calculate ψ because the stellar inclination is not known. Instead, assuming that the stellar inclination is drawn from an isotropic distribution, uniform in $\cos i_*$, we use the above equation to determine the possible values of ψ and their relative probabilities. For our derived posteriors on λ and i , we find that the orbit is indeed retrograde (that is, $\psi > 90^\circ$) at 99.5% confidence in this scenario, and we calculate the obliquity to be $\psi = 141_{-24}^{+15}$. This value is consistent with expectations for vZLK-driven migration; simulations show that the final obliquity can be as large as 180° for systems such as this⁷. This is not definitive proof of the formation history, however, as retrograde orbits such as this can also be produced through planet–planet interactions^{108,109}. Regardless, we warn that our result is strongly dependent on the naive assumption of an isotropic stellar inclination distribution, which is not always valid^{110,111}.

Dynamical history—analytic constraints

The high eccentricity and tight orbit of TIC 241249530 b and the presence of the distant stellar binary companion indicate a likely history of high-eccentricity migration driven by vZLK oscillations and tidal dissipation. To determine how this formation channel could have delivered the exoplanet to its current orbit, we first identify a set of initial conditions consistent with the present-day architecture of the system. We work in the context of the secular approximation for the evolution of hierarchical triple configurations¹¹².

The planet is at present close enough to the primary star such that short-range forces—general relativity (GR), tides and rotational distortions—have quenched any vZLK oscillations driven by the

companion. We calculate the semimajor axis at which this quenching occurs by assuming that GR dominates the short-range forces and examining the ratio between the timescale of GR precession of the inner orbit and the timescale for vZLK oscillations. To leading order (quadrupole limit), this ratio is¹¹³

$$\frac{t_{\text{GR}}}{t_{\text{quad}}} = \frac{a^4}{3a_2^3} \frac{(1-e^2)M_2c^2}{(1-e^2)^{3/2}G(M_*+M_p)^2}$$

in which M_* is the mass of the primary star; M_p , a and e are the mass, semimajor axis and eccentricity of the planet; and M_2 , a_2 and e_2 are the mass, semimajor axis and eccentricity of the binary companion. For the exoplanet and primary-star parameters, we adopt the median posteriors from our joint fit. For the binary companion, we set $M_2 = 0.453 M_\odot$, $a_2 = 1.664$ AU and $e_2 = 0.5$. If the planet started with a low initial eccentricity of $e = 0.1$, vZLK oscillations would have started only if the initial semimajor axis of the planet was $a_i > 4.2$ AU, for which this value is calculated by setting $t_{\text{GR}}/t_{\text{quad}} = 1$.

We can now constrain the initial eccentricity by requiring that the periastron distance of the first vZLK oscillation was sufficiently small to trigger efficient tidal dissipation. In particular, in the quadrupole limit, the quantity $a_f \equiv a(1 - e_{\text{max}}^2)$ is approximately conserved throughout the tidal migration, as the orbital angular momentum is conserved both during episodes of maximum eccentricity, as well as after vZLK oscillations have been quenched. Here e_{max} indicates the maximum eccentricity reached during a vZLK oscillation and a_f is equal to the final semimajor axis once the orbit has fully circularized. If a_f is taken to be conserved, the maximum eccentricity of the initial vZLK oscillation must have been $e_{i,\text{max}} > 0.9947$.

Exciting an eccentricity this high on the initial vZLK oscillation must have required a substantial initial inclination, I_i , between the orbit of the planet and that of the binary companion. We derive a lower bound on I_i using the following equation from ref. 112:

$$\epsilon_{\text{GR}} \left(\frac{1}{j_{i,\text{min}}} - 1 \right) = \frac{9 e_{i,\text{max}}^2}{8 j_{i,\text{min}}^2} \left(j_{i,\text{min}}^2 - \frac{5}{3} \cos^2 I_i \right).$$

Here $j_{i,\text{min}} = \sqrt{1 - e_{i,\text{max}}^2}$ and we have assumed GR perturbations to be dominant over those from tidal and rotational distortion. The dimensionless quantity ϵ_{GR} measures the ‘strength’ of perturbations from GR relative to those of the binary companion and it is defined as

$$\epsilon_{\text{GR}} \equiv 3G(M_* + M_p)^2 a_2^3 (1 - e_2^2)^{3/2} / (M_2 a^4 c^2).$$

Extended Data Fig. 5 shows the required initial inclination between the planetary and binary orbital planes and the resulting initial maximum eccentricity with respect to the initial semimajor axis of the planet. Although vZLK oscillations are present when $a_i > 4.2$ AU, not all values above this threshold yield defined values for I_i because the short-range forces are too strong for the planet to reach the required high initial eccentricity unless the initial semimajor axis exceeds $a_i > 7.0$ AU. The maximum eccentricity of the initial vZLK cycle must have been $e_{i,\text{max}} > 0.9947$ to generate the present-day semimajor axis and eccentricity. Attaining a maximum eccentricity this large is only possible with a nearly polar initial inclination between the orbit planes of the planet and the binary companion. We find that the initial inclination $I_i > 86.8^\circ$ for $a_i > 7.0$ AU. Altogether, these results indicate that it is possible to reach the present-day parameters of the system if the planet started beyond $a_i > 7.0$ AU and the binary companion started on an orbit nearly perpendicular to that of the planet.

Dynamical history—simulations

We now use our derived constraints on the initial orbital conditions to explore the planetary orbital evolution through numerical simulations.

Article

We conduct integrations of the secular equations of motion for TIC 241429530 through KozaiPy, a publicly available software package that simulates hierarchical three-body systems (<https://github.com/djmunoz/kozai.py>). The equations of motion are provided in ref. 3. We adopt initial values of $a_i = 10$ AU and $e_i = 0.1$, considering the minimum semimajor axis necessary for vZLK oscillations to be present. We consider perturbations to the octupole order and also account for tidal evolution in the constant-time-lag model of equilibrium tides¹¹⁴. Tidal parameters are adjusted so that the system reaches its present-day orbital parameters at an age of 3 Gyr, approximately equal to the derived age of the system. Specifically, the Love number of the planet is set to $k_2 = 0.25$ and its viscous timescale is set to $t_v = 0.01$ days.

The simulation results are presented in Extended Data Fig. 6. They indicate the presence of vZLK oscillations that trigger periods of very large eccentricities. At the times that the periape distance is minimized, tidal dissipation is strong and the semimajor axis shrinks. Eventually, the semimajor axis becomes small enough that the vZLK oscillations are suppressed owing to short-range forces and the planet decouples from the binary companion. After the vZLK oscillations are quenched, the mutual inclination is approximately conserved and the eccentricity of the planet slowly damps owing to continued tidal dissipation. We observe that there is an instant in time at which the eccentricity and semimajor axis of the planet are very close to the present-day values. We also note that the value of $a(1 - e_{\max}^2)$ is conserved during episodes of maximum eccentricity of each individual vZLK cycle, ranging within only a few percent of the average value of $a(1 - e_{\max}^2)$. According to this simulation, continued dissipation will cause the planet to reach a circular orbit in about a billion years. Altogether, this simulation provides a plausible proof of concept of the system's dynamical history of coupled vZLK oscillations and tidal migration. We suggest future work on the system to explore the role that dynamical tides might have played in its formation.

Modelling the transiting-warm-Jupiter eccentricity distribution

To explore the relation between exoplanet mass and eccentricity for warm Jupiters, or intermediate-period giant planets, we start with the sample of all transiting exoplanets with masses between 0.3 and 15 times that of Jupiter and orbital periods between 10 and 365 days. For each system in this sample, we adopt the most up-to-date mass and eccentricity constraints for which the eccentricity was fit as a free parameter when solving for the orbit. We discard four planets for which all literature solutions assumed a circular orbit with the eccentricity fixed at 0. All of these planets are less than 1.3 Jupiter masses. We also remove two planets in P-type circumbinary orbits, as the dynamical environments of these systems are expected to differ from those of planets orbiting single stars^{115,116}. Our sample differs from that analysed in ref. 41, which draws from the RV planet sample and thus uses projected planet mass ($M_p \sin i$) instead of true mass. By restricting our analysis to transiting exoplanets, we ensure that the measured masses are not degenerate with orbital inclination. This approach also mitigates the susceptibility of our results to detection biases, as the completeness fractions of transit surveys should be largely insensitive to exoplanet mass in the Jupiter-sized-planet regime.

The median mass of our sample is 1.935 Jupiter masses. We divide the sample into two groups of equal size, placing planets more massive than the median into one group and planets less massive than the median into the other group. The population-level eccentricity distribution of each group is then modelled in PyMC¹¹⁷ using a hierarchical Bayesian framework. For our model, we adopt a beta distribution with two hyperparameters, $\theta = \{\mu, \kappa\}$, in which μ describes the mean of the distribution and $1/\kappa$ describes its variance. These hyperparameters represent a reparameterization of the standard beta distribution parameters α and β , in which $\alpha = \mu\kappa$ and $\beta = (1 - \mu)\kappa$. A beta distribution is chosen for its flexibility in shape and because it is naturally bounded between 0 and 1. We adopt a uniform hyperprior for $\mu \sim U(0, 1)$ and a

log-normal hyperprior for $\log \kappa \sim N(0, 3)$. These choices reduce the impact of hyperprior choices on the inference results, especially when the sample size is small, as is the case here¹¹⁸. The best-fit distributions are shown in Fig. 3 and the resulting hyperparameters are $\mu_{\text{low}} = 0.18_{-0.03}^{+0.04}$, $\log \kappa_{\text{low}} = 1.23_{-0.29}^{+0.27}$, $\mu_{\text{high}} = 0.44_{-0.05}^{+0.05}$ and $\log \kappa_{\text{high}} = 0.91_{-0.24}^{+0.22}$. The mean values, μ , of the eccentricity distributions of low-mass and high-mass transiting warm Jupiters differ by 4.2σ . To assess the robustness of this result, we repeated the process for mass cutoffs between 1 Jupiter mass and 2.7 Jupiter masses. These bounds were chosen such that the size ratio of the two groups does not exceed 2:1. At each cutoff, we ran 1,000 trials, drawing the planet masses from asymmetric Gaussian distributions with means and widths determined by their literature values and uncertainties. For all mass-cutoff values over this range, the mean values of the two eccentricity distributions differ by $3-5\sigma$.

Data availability

The TESS data products referenced and analysed in this work are publicly available through the Mikulski Archive for Space Telescopes (MAST) at <https://exo.mast.stsci.edu/>. The raw NEID, HPF and HARPS-N spectra are available on request. Source data are provided with this paper.

Code availability

AstroImageJ is publicly available and can be downloaded at https://www.astro.louisville.edu/software/astroimagej/installation_packages/. The exoplanet software package is open source and public and can be downloaded at <https://github.com/exoplanet-dev/exoplanet>. The PyMC software package is open source and public and can be downloaded at <https://github.com/pymc-devs/pymc>.

- Huang, C. X. et al. Photometry of 10 million stars from the first two years of TESS full frame images: part I. *Res. Notes Am. Astron. Soc.* **4**, 204 (2020).
- Huang, C. X. et al. Photometry of 10 million stars from the first two years of TESS full frame images: part II. *Res. Notes Am. Astron. Soc.* **4**, 206 (2020).
- Gupta, A. F. et al. A high-eccentricity warm Jupiter orbiting TOI-4127. *Astron. J.* **165**, 234 (2023).
- Harris, M. et al. Separated twins or just siblings? A multiplanet system around an M dwarf including a cool sub-Neptune. *Astrophys. J. Lett.* **959**, L1 (2023).
- Mann, C. R. et al. Giant Outer Transiting Exoplanet Mass (GOT-EM) Survey. III. Recovery and confirmation of a temperate, mildly eccentric, single-transit Jupiter orbiting TOI-2010. *Astron. J.* **166**, 239 (2023).
- Mireles, I. et al. TOI-4600 b and c: two long-period giant planets orbiting an early K dwarf. *Astrophys. J. Lett.* **954**, L15 (2023).
- Smith, J. C. et al. Kepler Presearch Data Conditioning II - a Bayesian approach to systematic error correction. *Publ. Astron. Soc. Pac.* **124**, 1000 (2012).
- Stumpe, M. C. et al. Kepler Presearch Data Conditioning I—architecture and algorithms for error correction in Kepler light curves. *Publ. Astron. Soc. Pac.* **124**, 985 (2012).
- Stumpe, M. C. et al. Multiscale systematic error correction via wavelet-based bandsplitting in Kepler data. *Publ. Astron. Soc. Pac.* **126**, 100 (2014).
- Jenkins, J. M. et al. The TESS science processing operations center. *Proc. SPIE* **9913**, 99133E (2016).
- Caldwell, D. A. et al. TESS science processing operations center FFI target list products. *Res. Notes Am. Astron. Soc.* **4**, 201 (2020).
- Howell, S. B. et al. Speckle camera observations for the NASA Kepler Mission Follow-up Program. *Astron. J.* **142**, 19 (2011).
- Marchis, F. et al. Unistellar eVscopes: smart, portable, and easy-to-use telescopes for exploration, interactive learning, and citizen astronomy. *Acta Astronaut.* **166**, 23–28 (2020).
- Dalba, P. A. & Muirhead, P. S. No timing variations observed in third transit of snow-line exoplanet Kepler-421b. *Astrophys. J. Lett.* **826**, L7 (2016).
- Dalba, P. A. et al. Kepler transit depths contaminated by a phantom star. *Astron. J.* **153**, 59 (2017).
- Stefánsson, G. et al. Extreme precision photometry from the ground with beam-shaping diffusers for K2, TESS, and beyond. *Proc. SPIE* **10702**, 1070250 (2018).
- Collins, K. A. et al. AstroImageJ: image processing and photometric extraction for ultra-precise astronomical light curves. *Astron. J.* **153**, 77 (2017).
- Stefánsson, G. et al. Diffuser-assisted photometric follow-up observations of the Neptune-sized planets K2-28b and K2-100b. *Astron. J.* **156**, 266 (2018).
- Baranne, A. et al. ELODIE: a spectrograph for accurate radial velocity measurements. *Astron. Astrophys. Suppl. Ser.* **119**, 373–390 (1996).
- Zechmeister, M. et al. Spectrum radial velocity analyser (SERVAL). High-precision radial velocities and two alternative spectral indicators. *Astron. Astrophys.* **609**, A12 (2018).
- Anglada-Escudé, G. & Butler, R. P. The HARPS-TERRA project. I. Description of the algorithms, performance, and new measurements on a few remarkable stars observed by HARPS. *Astrophys. J. Suppl. Ser.* **200**, 15 (2012).

63. Stefánsson, G. et al. The warm Neptune GJ 3470b has a polar orbit. *Astrophys. J. Lett.* **931**, L15 (2022).
64. Ramsey, L. W. et al. Early performance and present status of the Hobby-Eberly Telescope. *Proc. SPIE* **3352**, 34–42 (1998).
65. Hill, G. J. et al. The HETDEX instrumentation: Hobby-Eberly telescope wide-field upgrade and VIRUS. *Astron. J.* **162**, 298 (2021).
66. Ninan, J. P. et al. The Habitable-Zone Planet Finder: improved flux image generation algorithms for H2RG up-the-ramp data. *Proc. SPIE* **10709**, 107092U (2018).
67. Kanodia, S. & Wright, J. Python leap second management and implementation of precise barycentric correction (barycorrpy). *Res. Notes Am. Astron. Soc.* **2**, 4 (2018).
68. Metcalf, A. J. et al. Stellar spectroscopy in the near-infrared with a laser frequency comb. *Optica* **6**, 233–239 (2019).
69. Stefánsson, G. et al. A Neptune-mass exoplanet in close orbit around a very low-mass star challenges formation models. *Science* **382**, 1031–1035 (2023).
70. Hunter, A. A. et al. Yabi: an online research environment for grid, high performance and cloud computing. *Source Code Biol. Med.* **7**, 1 (2012).
71. Blanco-Cuaresma, S. et al. Determining stellar atmospheric parameters and chemical abundances of FGK stars with iSpec. *Astron. Astrophys.* **569**, A111 (2014).
72. Blanco-Cuaresma, S. Modern stellar spectroscopy caveats. *Mon. Not. R. Astron. Soc.* **486**, 2075–2101 (2019).
73. Gray, R. O. & Corbally, C. J. The calibration of MK spectral classes using spectral synthesis. I: the effective temperature calibration of dwarf stars. *Astron. J.* **107**, 742–746 (1994).
74. Gustafsson, B. et al. A grid of MARCS model atmospheres for late-type stars. I. Methods and general properties. *Astron. Astrophys.* **486**, 951–970 (2008).
75. Grevesse, N., Asplund, M. & Sauval, A. J. The solar chemical composition. *Space Sci. Rev.* **130**, 105–114 (2007).
76. Heiter, U. et al. Atomic data for the Gaia-ESO Survey. *Astron. Astrophys.* **645**, A106 (2021).
77. Blanco-Cuaresma, S. et al. The Gaia FGK benchmark stars. High resolution spectral library. *Astron. Astrophys.* **566**, A98 (2014).
78. Masseron, T., Merle, T., & Hawkins, K., BACCHUS: Brussels Automatic Code for Characterizing High accuracy Spectra. Astrophysics Source Code Library, record ascl:1605.004 (2016).
79. Alvarez, R. & Plez, B. Near-infrared narrow-band photometry of M-giant and Mira stars: models meet observations. *Astron. Astrophys.* **330**, 1109–1119 (1998).
80. Plez, B., Turbospectrum: code for spectral synthesis. Astrophysics Source Code Library, record ascl:1205.004 (2012).
81. Stassun, K. G. & Torres, G. Eclipsing binary stars as benchmarks for trigonometric parallaxes in the Gaia era. *Astron. J.* **152**, 180 (2016).
82. Stassun, K. G., Collins, K. A. & Gaudi, B. S. Accurate empirical radii and masses of planets and their host stars with Gaia parallaxes. *Astron. J.* **153**, 136 (2017).
83. Stassun, K. G. et al. Empirical accurate masses and radii of single stars with TESS and Gaia. *Astron. J.* **155**, 22 (2018).
84. Cutri, R. M. et al. VizieR Online Data Catalog: 2MASS All-Sky Catalog of Point Sources (Cutri+ 2003). VizieR Online Data Catalog, 2246, II/246 (2003).
85. Wright, E. L. et al. The Wide-field Infrared Survey Explorer (WISE): mission description and initial on-orbit performance. *Astron. J.* **140**, 1868–1881 (2010).
86. Gaia Collaboration, et al. Gaia Data Release 3. A golden sample of astrophysical parameters. *Astron. Astrophys.* **674**, A39 (2023).
87. Henden, A. A. et al. APASS Data Release 10. American Astronomical Society Meeting Abstracts #232, 223.06 (2018).
88. Martin, D. C. et al. The Galaxy Evolution Explorer: a space ultraviolet survey mission. *Astrophys. J.* **619**, L1–L6 (2005).
89. Husser, T.-O. et al. A new extensive library of PHOENIX stellar atmospheres and synthetic spectra. *Astron. Astrophys.* **553**, A6 (2013).
90. Schlegel, D. J., Finkbeiner, D. P. & Davis, M. Maps of dust infrared emission for use in estimation of reddening and cosmic microwave background radiation foregrounds. *Astrophys. J.* **500**, 525–553 (1998).
91. Torres, G., Andersen, J. & Giménez, A. Accurate masses and radii of normal stars: modern results and applications. *Astron. Astrophys. Rev.* **18**, 67–126 (2010).
92. Demarque, P. et al. Y^2 isochrones with an improved core overshoot treatment. *Astrophys. J. Suppl. Ser.* **155**, 667–674 (2004).
93. Hedges, C. et al. Systematics-insensitive periodogram for finding periods in TESS observations of long-period rotators. *Res. Notes Am. Astron. Soc.* **4**, 220 (2020).
94. Pollacco, D. L. et al. The WASP project and the SuperWASP cameras. *Publ. Astron. Soc. Pac.* **118**, 1407–1418 (2006).
95. El-Badry, K., Rix, H.-W. & Heintz, T. M. A million binaries from Gaia eDR3: sample selection and validation of Gaia parallax uncertainties. *Mon. Not. R. Astron. Soc.* **506**, 2269–2295 (2021).
96. Mann, A. W. et al. How to constrain your M dwarf. II. The mass–luminosity–metallicity relation from 0.075 to 0.70 solar masses. *Astrophys. J.* **871**, 63 (2019).
97. Giovinazzi, M. R. & Blake, C. H. A mass–magnitude relation for low-mass stars based on dynamical measurements of thousands of binary star systems. *Astron. J.* **164**, 164 (2022).
98. Foreman-Mackey, D. et al. exoplanet: gradient-based probabilistic inference for exoplanet data & other astronomical time series. *J. Open Source Softw.* **6**, 3285 (2021).
99. Luger, R. et al. starry: analytic occultation light curves. *Astron. J.* **157**, 64 (2019).
100. Agol, E., Luger, R. & Foreman-Mackey, D. Analytic planetary transit light curves and derivatives for stars with polynomial limb darkening. *Astron. J.* **159**, 123 (2020).
101. Mandel, K. & Agol, E. Analytic light curves for planetary transit searches. *Astrophys. J.* **580**, L171–L175 (2002).
102. Salvatier, J., Wiecki, T. V., & Fonnesbeck, C. PyMC3: Python probabilistic programming framework. Astrophysics Source Code Library, record ascl:1610.016 (2016).
103. Dong, J. et al. Warm Jupiters in TESS full-frame images: a catalog and observed eccentricity distribution for year 1. *Astrophys. J. Suppl. Ser.* **255**, 6 (2021).
104. Kipping, D. M. Efficient, uninformative sampling of limb darkening coefficients for two-parameter laws. *Mon. Not. R. Astron. Soc.* **435**, 2152–2160 (2013).
105. Burt, J. A. et al. TOI-824 b: a new planet on the lower edge of the hot Neptune desert. *Astron. J.* **160**, 153 (2020).
106. Lin, A. S. J. et al. The unusual M-dwarf Warm Jupiter TOI-1899 b: refinement of orbital and planetary parameters. *Astron. J.* **166**, 90 (2023).
107. Hirano, T. et al. Improved Modeling of the Rossiter-McLaughlin Effect for Transiting Exoplanets. *Astrophys. J.* **742**, 69 (2011).
108. Naoz, S. et al. Hot Jupiters from secular planet–planet interactions. *Nature* **473**, 187–189 (2011).
109. Li, G. et al. Eccentricity growth and orbit flip in near-coplanar hierarchical three-body systems. *Astrophys. J.* **785**, 116 (2014).
110. Ho, S. & Turner, E. L. The posterior distribution of $\sin(i)$ values for exoplanets with $M_J \sin(i)$ determined from radial velocity data. *Astrophys. J.* **739**, 26 (2011).
111. Morton, T. D. & Johnson, J. A. Discerning exoplanet migration models using spin–orbit measurements. *Astrophys. J.* **729**, 138 (2011).
112. Naoz, S. The eccentric Kozai-Lidov effect and its applications. *Annu. Rev. Astron. Astrophys.* **54**, 441–489 (2016).
113. Liu, B., Muñoz, D. J. & Lai, D. Suppression of extreme orbital evolution in triple systems with short-range forces. *Mon. Not. R. Astron. Soc.* **447**, 747–764 (2015).
114. Leconte, J. et al. Is tidal heating sufficient to explain bloated exoplanets? Consistent calculations accounting for finite initial eccentricity. *Astron. Astrophys.* **516**, A64 (2010).
115. Holman, M. J. & Wiegert, P. A. Long-term stability of planets in binary systems. *Astron. J.* **117**, 621–628 (1999).
116. Piersens, A. & Nelson, R. P. On the formation and migration of giant planets in circumbinary discs. *Astron. Astrophys.* **483**, 633–642 (2008).
117. Wiecki, T. et al. pymc-devs/pymc: v5.0.1. *Zenodo* <https://doi.org/10.5281/zenodo.4603970> (2022).
118. Dong, J. & Foreman-Mackey, D. A hierarchical Bayesian framework for inferring the stellar obliquity distribution. *Astron. J.* **166**, 112 (2023).
119. Stassun, K. G. et al. The TESS input catalog and candidate target list. *Astron. J.* **156**, 102 (2018).

Acknowledgements A.F.G. thanks B. Dawson and J. Najita for guidance. NEID is financed by the National Aeronautics and Space Administration (NASA) through the Jet Propulsion Laboratory (JPL) by contract 1547612 and the NEID Data Reduction Pipeline is financed through JPL contract 1644767. Funding for this work was partially provided by Research Support Agreements 1646897 and 1679618 administered by JPL. The Center for Exoplanets and Habitable Worlds and the Penn State Extraterrestrial Intelligence Center are supported by the Pennsylvania State University and the Eberly College of Science. This research has made use of the SIMBAD database, operated at Strasbourg astronomical Data Center (CDS), Strasbourg, France, and NASA's Astrophysics Data System Bibliographic Services. This research was carried out, in part, at JPL, California Institute of Technology, under a contract with NASA (80NMO018D0004). Computations for this research were performed on the Pennsylvania State University's Institute for Computational and Data Sciences Advanced Cyberinfrastructure (ICDS-ACI). This content is solely the responsibility of the authors and does not necessarily represent the views of the Institute for Computational and Data Sciences. This paper contains data taken with the NEID instrument, which was financed by the NASA-NSF Exoplanet Observational Research (NN-EXPLORE) partnership and built by Pennsylvania State University. NEID is installed on the WIYN telescope, which is operated by the National Science Foundation (NSF)'s National Optical-Infrared Astronomy Research Laboratory, and the NEID archive is operated by the NASA Exoplanet Science Institute at the California Institute of Technology. Some of the observations in this paper made use of the NN-EXPLORE Exoplanet Stellar Speckle Imager (NESSI). NESSI was financed by the NASA Exoplanet Exploration Program and the NASA Ames Research Center. NESSI was built at the Ames Research Center by S. B. Howell, N. Scott, E. P. Horch and E. Quigley. NN-EXPLORE is managed by JPL, California Institute of Technology under contract with NASA. This work includes data collected by the TESS mission, which are publicly available from the Mikulski Archive for Space Telescopes (MAST). Funding for the TESS mission is provided by the NASA Science Mission Directorate. We acknowledge the use of public TESS data from pipelines at the TESS Science Office and at the TESS Science Processing Operations Center. Resources supporting this work were provided by the NASA High-End Computing (HEC) Program through the NASA Advanced Supercomputing (NAS) Division at Ames Research Center for the production of the SPOC data products. This research has made use of the Exoplanet Follow-up Observing Program website, which is operated by the California Institute of Technology, under contract with NASA under the Exoplanet Exploration Program. Some of the data presented in this paper were obtained from MAST. Support for MAST for non-HST data is provided by the NASA Office of Space Science through grant NNX09AF08G and by other grants and contracts. This work has made use of data from the European Space Agency (ESA) mission Gaia, processed by the Gaia Data Processing and Analysis Consortium (DPAC). Funding for the DPAC has been provided by national institutions, in particular the institutions participating in the Gaia Multilateral Agreement. This research has made use of the NASA Exoplanet Archive, which is operated by the California Institute of Technology, under contract with NASA under the Exoplanet Exploration Program. This research was made possible through the use of the AAVSO Photometric All-Sky Survey (APASS), financed by the Robert Martin Ayers Sciences Fund and NSF AST-1412587. We thank N. Leroux for assistance with the Unistellar observations. C.I.C. acknowledges support by NASA Headquarters through an appointment to the NASA Postdoctoral Program at Goddard Space Flight Center, administered by ORAU through a contract with NASA. W.D.C. acknowledges financial support from the NSF through grant AST-2108801. E.P. and I.C. acknowledge financial support from the Agencia Estatal de Investigación of the Ministerio de Ciencia e Innovación MCIN/AEI/10.13039/501100011033 and the ERDF 'A way of making Europe' through project PID2021-125627OB-C32 and from the Centre of Excellence 'Severo Ochoa' award to the Instituto de Astrofísica de Canarias. C.X.H. thanks the support of the ARC DECRA project DE200101840. G.N. acknowledges research funding from the Ministry of Education and Science programme the 'Excellence Initiative – Research University' conducted at the Centre of Excellence in Astrophysics and Astrochemistry of the Nicolaus Copernicus University in Toruń, Poland. T.M. acknowledges financial support from the Spanish Ministry of Science and Innovation (MICINN) through the Spanish State Research Agency, under the Severo Ochoa Program 2020–2023 (CEX2019-000920-S). D.D. acknowledges support from the NASA Exoplanet Research Program grant 18-2XRPI8_2-0136

Article

and from the TESS Guest Investigator Program grant 80NSSC23K0769. G. Stefánsson acknowledges support provided by NASA through the NASA Hubble Fellowship grant HST-HF2-51519.001-A awarded by the Space Telescope Science Institute, which is operated by the Association of Universities for Research in Astronomy, Inc., for NASA, under contract NAS5-26555. Based in part on observations at Kitt Peak National Observatory, NSF's NOIRLab (proposal IDs 2021A-0388, 2021B-0442, 2022A-627532, 2022B-176691, 2023A-383728, 2023A-722344, 2023B-607177 and 2024A-843425; PI: A. Gupta), managed by the Association of Universities for Research in Astronomy (AURA) under a cooperative agreement with the NSF. We thank the WIYN Observing Associates for their support of our NEID observations. We are honoured to be permitted to conduct astronomical research on Iolkam Du'ag (Kitt Peak), a mountain with particular importance to the Tohono O'odham. We also thank Z. Arnold, J. Davis, M. Edwards, J. Ehret, T. Juan, B. Pisarek, A. Rowe, F. Wortman, the Eastern Area Incident Management Team and all of the firefighters and air support crew who fought the recent Contreras Fire and saved Kitt Peak National Observatory. These results are based on observations obtained with the Habitable-zone Planet Finder Spectrograph on the Hobby-Eberly Telescope (HET). The HPF team acknowledges support from NSF grants AST-1006676, AST-1126413, AST-1310885, AST-1517592, AST-1310875, ATI 2009889, ATI-2009982 and AST-2108512 as well as the NASA Astrobiology Institute (NNA09DA76A) in the pursuit of precision radial velocities in the near-infrared. The HPF team also acknowledges support from the Heising-Simons Foundation through grant 2017-0494. The HET is a joint project of the University of Texas at Austin, the Pennsylvania State University, Ludwig-Maximilians-Universität München and Georg-August Universität Göttingen. The HET is named in honour of its principal benefactors, W. P. Hobby and R. E. Eberly. The Texas Advanced Computing Center (TACC) at the University of Texas at Austin provided high-performance computing, visualization and storage resources that have contributed to the results reported in this paper. C.I.C. and S.V. are NASA Postdoctoral Fellows. B.G., R.K., L.L., M.L., M.P., M.S., G. Simard and S.W. are Unistellar Citizen Scientists. G. Stefánsson is a NASA Sagan Fellow.

Author contributions A.F.G. selected TIC241249530 for ground-based observations, designed and led the NEID, NESSI and HPF observing programmes, performed the transit and radial velocity analysis, coordinated the analysis of the transiting-warm-Jupiter mass–eccentricity distribution and wrote most of the manuscript. S.C.M. and H.I. performed the analysis of the dynamical history and trajectory of TIC241249530 b and contributed the associated text and figures. J.D. wrote the code to analyse the eccentricity distributions and contributed to the theoretical interpretation of the results. J.M.J. contributed to the theoretical interpretation of

the eccentricity distribution results. I.C. helped coordinate the HARPS-N observations. J.L.-R., M.D. and S.M. coordinated and conducted the ARCTIC observations and data processing. M.R.G. contributed to the characterization of TIC241249532. A.S.J.L. performed the SERVAL analysis of the NEID spectra and S.K. performed the SERVAL analysis of the HPF spectra. X.-Y.W. performed the iSpec analysis of the NEID spectra. D.D. coordinated the efforts of the TESS Single Transit Planet Candidate Working Group. K.S. performed the SED analysis. D.J.S. ran an independent analysis of the stellar SED to validate the results. T.M. performed the BACCHUS analysis of the HARPS-N spectra. S.M. and J. Wright contributed to the interpretation of the significance of the TIC241249530 system in the context of the exoplanet population and to the coordination of follow-up observations. M.E.E. conducted the NESSI observations, generated the reconstructed speckle images and calculated the contrast limits. S.E.L., H.S., E.G., J.H., J.K., P.F. and Y.P. scheduled and executed the NEID observations. J.A.A.-M., C.B., C.H.B., C.I.C., S.H., S.K., A.S.J.L., S.M., M.W.M., A.M., J.P.N., J.R., P.R., A.R., C.S., G. Stefánsson and J. Wright contributed to the design, development and commissioning of the NEID spectrograph and data-reduction software. C.B., W.D.C., S.K., J.P.N., P.R., A.R. and G. Stefánsson contributed to the design, development and commissioning of the HPF spectrograph and data-reduction software. D.P.S. assisted with the coordination of the HPF observations. G.N. and E.P. coordinated and conducted the HARPS-N observations. L.H. contributed to the development and installation of the diffuser used to obtain the ARCTIC observations. L.H. and J. Wisniewski helped coordinate and execute the ARCTIC observations. S.V. developed the pipeline with which the TESS transit signal for TIC241249530 b was first detected and P.D., J.P. and C.Z. vetted the alerted signals in TESS Sector 20 and helped validate the transit of TIC241249530 b. C.X.H. developed the Quick Look Pipeline and D.C. developed the TESS-SPOC pipeline. B.G., R.K., L.L., M.L., M.P., M.S. and G. Simard conducted the Unistellar observations and L.S. analysed the Unistellar data.

Competing interests The authors declare no competing interests.

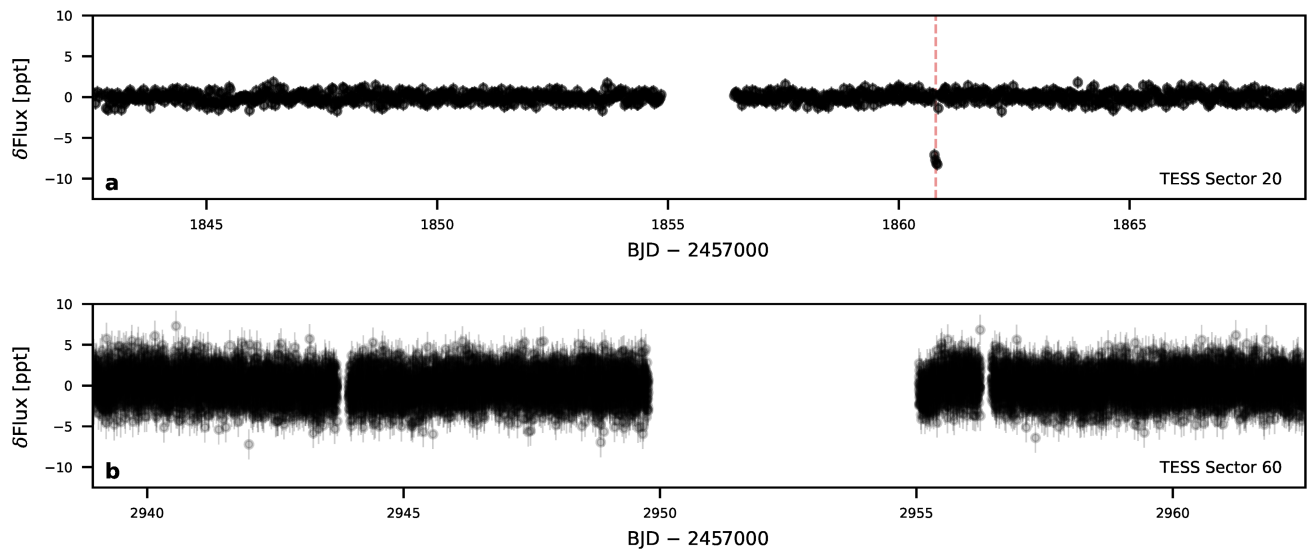
Additional information

Supplementary information The online version contains supplementary material available at <https://doi.org/10.1038/s41586-024-07688-3>.

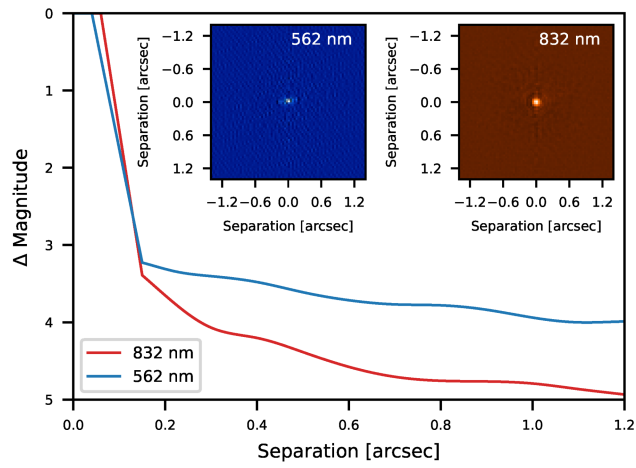
Correspondence and requests for materials should be addressed to Arvind F. Gupta.

Peer review information *Nature* thanks Daniel Fabrycky and Artie Hatzes for their contribution to the peer review of this work. Peer reviewer reports are available.

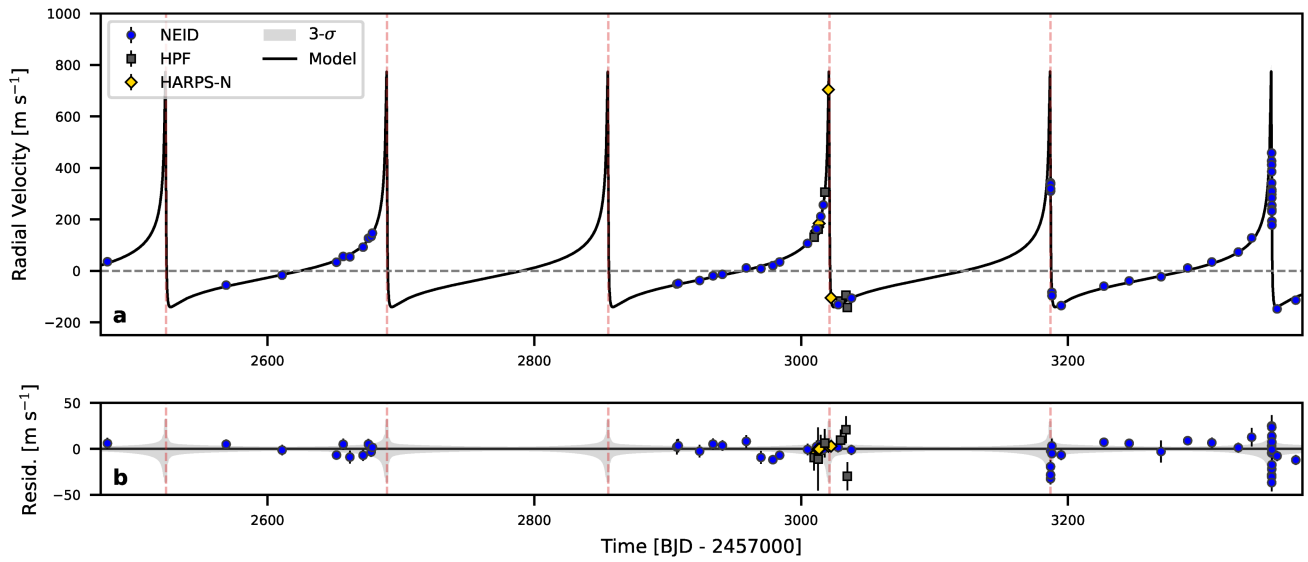
Reprints and permissions information is available at <http://www.nature.com/reprints>.



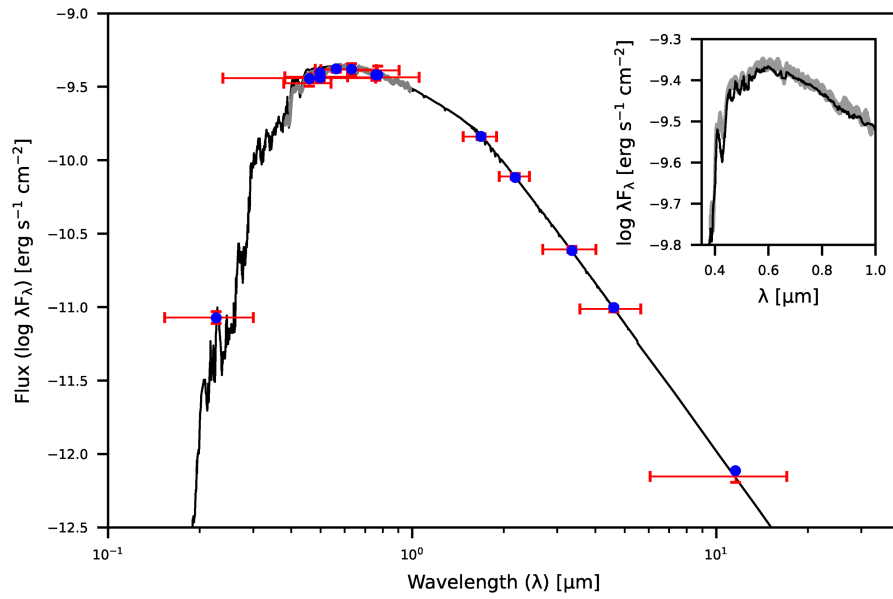
Extended Data Fig. 1 | TESS light curves for TIC 241249530. a, Sector 20 TESS-SPOC data (30-min cadence). The vertical dashed line marks the best-fit transit midpoint. **b**, Sector 60 SPOC data (2-min cadence). Error bars on individual points represent 1σ measurement uncertainties.



Extended Data Fig. 2 | Reconstructed NESSI speckle images and 5σ contrast curves for TIC 241249530. Observations were taken simultaneously at 562 nm with the blue camera (upper-left inset image) and at 832 nm with the red camera (upper-right inset image). The contrast curves indicate the limiting magnitude difference at which bound or background sources could be detected for separations between 0.2" and 1.2".

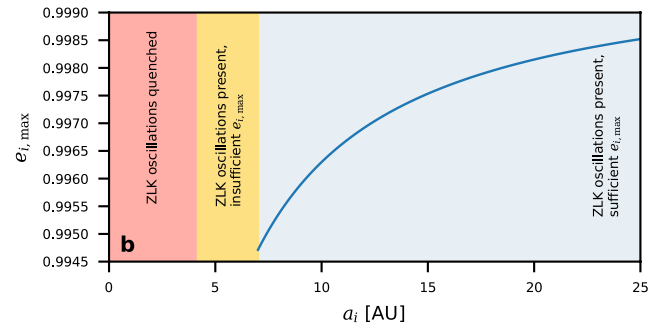
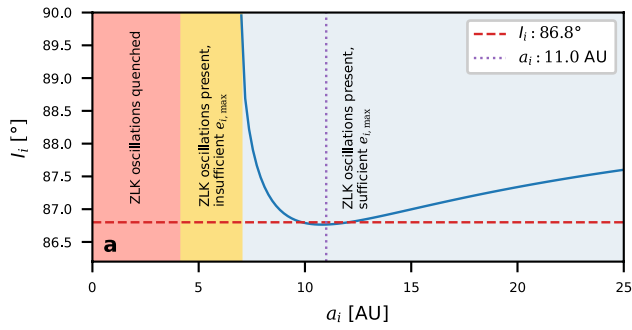


Extended Data Fig. 3 | RV time series for TIC241249530. **a**, RV measurements from NEID (blue), HPF (black) and HARPS-N (gold) and best-fit orbit model (black curve). **b**, Residuals to the RV orbit fit. Vertical red lines in both panels mark the predicted transit times. The grey-shaded region bounds the 3σ confidence intervals for the fit. The horizontal axis is in units of days relative to Barycentric Julian Date (BJD) 2457000. Error bars on individual points represent 1σ measurement uncertainties.



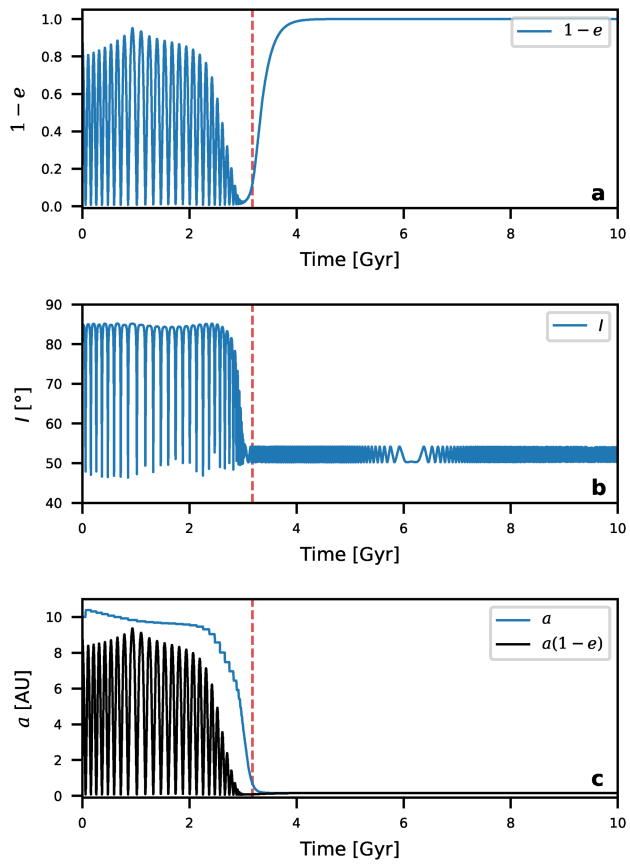
Extended Data Fig. 4 | SED for TIC 241249530. Red symbols represent the observed photometric measurements, for which the vertical error bars represent the 1σ measurement uncertainties and the horizontal bars represent

the effective width of the passband. Blue symbols are the model fluxes from the best-fit PHOENIX atmosphere model (black). The Gaia spectrophotometry is represented as a grey swathe (see also inset plot).



Extended Data Fig. 5 | Constraints on the parameters of the first vZLK oscillation for TIC 241249530 b. **a.** Constraints on initial inclination. **b.** Constraints on initial maximum eccentricity. The red region ($0 \text{ AU} < a_i < 4.2 \text{ AU}$) indicates the absence of vZLK oscillations. The orange region ($4.2 \text{ AU} < a_i < 7 \text{ AU}$) indicates the presence of vZLK oscillations but with insufficient $e_{i,\text{max}}$ to reach

the present-day orbit owing to strong short-range forces (primarily GR, with further contributions from tides and rotational distortions). The blue region ($a_i > 7 \text{ AU}$) indicates the presence of vZLK oscillations that can drive the planet to reach present-day parameters.



Extended Data Fig. 6 | Simulated evolution of the orbit of TIC 241249530 b resulting from high-eccentricity migration driven by vZLK oscillations. **a**, Evolution of the eccentricity of the planetary orbit over time. **b**, Evolution of the mutual inclination between the planet and binary orbits over time. **c**, Evolution of the semimajor axis, a , and periastron separation, $a(1 - e)$, of the planetary orbit over time. The vertical red lines at 3.2 Gyr mark the age at which the orbit reaches the present-day conditions ($e = 0.94$, $a = 0.64$ AU). We adopt $a_i = 10$ AU, $e_i = 0.1$ for the initial orbital parameters for illustrative purposes.

Extended Data Table 1 | Stellar parameters for TIC241249530 and TIC241249532

Parameter	Value		Unit	Ref.
Identifiers:				
TIC	241249530	241249532		119
<i>Gaia</i> DR3	995754258812449024	995754254517548032		86
2MASS	J06211411+5317423	J06211389+5317380		84
Coordinates and Parallax:				
R.A.	06:21:14.02	06:21:13.76	J2000	86
Dec	+53:17:42.32	+53:17:37.85	J2000	86
Parallax	2.96 ± 0.02	3.17 ± 0.09	mas	86
Proper Motion R.A.	7.620 ± 0.018	7.766 ± 0.107	mas yr ⁻¹	86
Proper Motion Dec	-15.717 ± 0.015	-15.799 ± 0.092	mas yr ⁻¹	86
Broadband photometry:				
<i>B</i>	12.226 ± 0.413		mag	87
<i>V</i>	11.689 ± 0.039		mag	87
TESS	11.1328 ± 0.0079	16.5809 ± 0.0314	mag	119
<i>G</i>	11.5593 ± 0.0003	17.4606 ± 0.0029	mag	86
<i>B_p</i>	11.8835 ± 0.0007	18.046 ± 0.090	mag	86
<i>R_p</i>	11.0698 ± 0.0005	16.054 ± 0.026	mag	86
<i>J</i>	10.538	12.017	mag	84
<i>H</i>	10.266 ± 0.024	13.741 ± 0.064	mag	84
<i>K_s</i>	10.192 ± 0.021	13.506 ± 0.071	mag	84
<i>W₁</i>	10.115 ± 0.023		mag	85
<i>W₂</i>	10.147 ± 0.021		mag	85
<i>W₃</i>	10.176 ± 0.065		mag	85
<i>W₄</i>	8.993		mag	85
Derived Stellar Parameters:				
<i>T_{eff}</i>	6166 ± 43		K	iSpec
	6150 ± 50		K	BACCHUS
log <i>g</i>	4.23 ± 0.06		log (cm s ⁻²)	iSpec
	4.25 ± 0.10		log (cm s ⁻²)	BACCHUS
[Fe/H]	0.09 ± 0.03		dex	iSpec
	0.20 ± 0.09		dex	BACCHUS
<i>v</i> sin <i>i_*</i>	4.2 ± 0.8		km s ⁻¹	iSpec
	5.5 ± 0.7		km s ⁻¹	BACCHUS
<i>M_*</i>	1.24 ± 0.07	0.453 ± 0.012	<i>M</i> _⊙	
<i>R_*</i>	1.404 ± 0.028		<i>R</i> _⊙	
<i>L_{*,bol}</i>	2.56 ± 0.08		<i>L</i> _⊙	
<i>F_{*,bol}</i>	7.19 ± 0.20 × 10 ⁻¹⁰		erg s ⁻¹ cm ⁻²	
Age	3.2 ± 0.5		Gyr	
<i>A_v</i>	0.31 ± 0.02		mag	

Data from refs. 84–87,119.

Extended Data Table 2 | Joint-fit priors and posteriors

Parameter	Prior	Posterior	Unit
Stellar Parameters:			
M_*	$\mathcal{N}(1.24, 0.07)$	$1.271^{+0.061}_{-0.068}$	M_\odot
R_*	$\mathcal{N}(1.404, 0.028)$	$1.397^{+0.025}_{-0.028}$	R_\odot
$v \sin i_*$	$\mathcal{N}(4.2, 0.8)$	$4.60^{+0.56}_{-0.63}$	km s^{-1}
ζ	$\mathcal{U}(2.0, 6.5)$	$3.6^{+1.7}_{-1.0}$	km s^{-1}
β	$\mathcal{U}(0.8, 1.2)$	$1.01^{+0.13}_{-0.12}$	km s^{-1}
γ	$\mathcal{U}(2.5, 4.5)$	$3.37^{+0.60}_{-0.54}$	km s^{-1}
$q_{1,\text{TESS}}$	$\mathcal{U}(0.0, 1.0)$	$0.35^{+0.29}_{-0.19}$	
$q_{2,\text{TESS}}$	$\mathcal{U}(0.0, 1.0)$	$0.17^{+0.29}_{-0.26}$	
$q_{1,\text{ARCTIC}}$	$\mathcal{U}(0.0, 1.0)$	$0.47^{+0.28}_{-0.23}$	
$q_{2,\text{ARCTIC}}$	$\mathcal{U}(0.0, 1.0)$	$0.14^{+0.40}_{-0.35}$	
$q_{1,\text{NEID}}$	$\mathcal{U}(0.0, 1.0)$	$0.48^{+0.39}_{-0.28}$	
$q_{2,\text{NEID}}$	$\mathcal{U}(0.0, 1.0)$	$-0.01^{+0.32}_{-0.26}$	
Orbital and Planetary Parameters:			
T_0	$\mathcal{N}(2458860.8, 0.01)$	$2458860.8007^{+0.0015}_{-0.0016}$	BJD
P	$\mathcal{N}(165.77, 0.1)$	$165.77190^{+0.00027}_{-0.00028}$	days
$\sqrt{e} \cos \omega$	$\mathcal{U}(-1.0, 1.0)$	$0.7174^{+0.0042}_{-0.0046}$	
$\sqrt{e} \sin \omega$	$\mathcal{U}(-1.0, 1.0)$	$0.6531^{+0.0050}_{-0.0046}$	
e	derived	$0.9412^{+0.0009}_{-0.0009}$	
ω	derived	$42.32^{+0.40}_{-0.36}$	deg
b	$\mathcal{U}(0.0, 1.0)$	$0.581^{+0.049}_{-0.058}$	
a	derived	$0.641^{+0.010}_{-0.012}$	AU
λ	$\mathcal{U}(-180, 180)$	$163.5^{+9.4}_{-7.7}$	deg
R_p/R_*	$\mathcal{U}(0.05, 0.15)$	$0.0873^{+0.0019}_{-0.0020}$	
M_p	$\mathcal{U}(0.5, 30)$	$4.98^{+0.16}_{-0.18}$	M_J
R_p	derived	$1.186^{+0.037}_{-0.040}$	R_J
Instrument Parameters:			
TESS Dilution	$\mathcal{U}(0.1, 1.2)$	$1.010^{+0.069}_{-0.067}$	
$\sigma_{\text{phot,TESS}}$	$\mathcal{L}(0.74, 10)$	$0.004^{+0.010}_{-0.004}$	ppt
$\sigma_{\text{phot,ARCTIC}}$	$\mathcal{L}(4.18, 10)$	$1.51^{+0.11}_{-0.10}$	ppt
$\sigma_{\text{RV,NEID-pre}}$	$\mathcal{U}(0, 25)$	$3.1^{+2.6}_{-1.9}$	m s^{-1}
$\sigma_{\text{RV,NEID-post}}$	$\mathcal{U}(0, 25)$	$4.6^{+1.6}_{-1.7}$	m s^{-1}
$\sigma_{\text{RV,HPF}}$	$\mathcal{U}(0, 25)$	$14.6^{+7.1}_{-8.4}$	m s^{-1}
$\sigma_{\text{RV,HARPS-N}}$	$\mathcal{U}(0, 25)$	$3.3^{+3.9}_{-2.1}$	m s^{-1}
$\gamma_{\text{RV,NEID-pre}}$	$\mathcal{N}(0, 1000)$	$-57.2^{+1.6}_{-1.6}$	m s^{-1}
$\gamma_{\text{RV,NEID-post}}$	$\mathcal{N}(0, 1000)$	$-70.1^{+1.3}_{-1.3}$	m s^{-1}
$\gamma_{\text{RV,HPF}}$	$\mathcal{N}(0, 1000)$	$-18.9^{+3.9}_{-4.1}$	m s^{-1}
$\gamma_{\text{RV,HARPS-N}}$	$\mathcal{N}(0, 1000)$	$-170.7^{+3.1}_{-2.7}$	m s^{-1}

We report the median values of the posterior distributions from our joint fit. Uncertainties represent the 68% confidence intervals ($\pm 1\sigma$) for each parameter. Limb darkening is sampled using the parameterization given by ref. 104. For λ , we use the custom angle distribution from the PyMC3 extras extension of the exoplanet package⁸⁸ to avoid discontinuities at $\pm\pi$.